Effects of Jet-Interaction on Pitch Control of a Launch Abort Vehicle

Michael J. Aftosmis† and **Stuart E. Rogers**‡
NASA Ames Research Center, Moffett Field, CA, 94035, USA

This work describes a series of high-fidelity computational studies examining the control authority of Attitude Control Motors (ACMs) for pitch control of an early candidate design of the Orion Launch Abort Vehicle (LAV). This study included both unsteady Reynolds-Averaged Navier-Stokes (RANS) and both steady and unsteady inviscid simulations. Over 50 overset RANS and 650 Cartesian Euler simulations were performed to characterize the aerodynamics of an early design for the Orion Pad-Abort LAV. These simulations spanned low-subsonic to high supersonic flight conditions and considered angle-of-attack variations from -30°to 50° and sideslip angles of 0° and 30°. Investigations of Jet Interaction (JI) showed that adverse JI occurs at positive angles-of-attack when the ACM jets screen the LAV tower from the oncoming flow. In particular, adverse JI causes ACM authority to drop dramatically at positive α over Mach numbers from 0.7-1.6, and can result in control reversal for some flight conditions. We briefly describe subsequent design modifications that can markedly improve control authority.

1 Introduction

SIMILAR to Apollo, the Orion Launch Abort Vehicle (LAV) consists of a tower mounted tractor rocket tasked with carrying the Crew Module (CM) safely away from the launch vehicle in the unlikely event of a catastrophic failure during the vehicle's ascent. The schematic in Figure 1 outlines the major components of this system on an early design of the Orion Pad-Abort test vehicle. Unlike the Apollo-era LAVs, the Orion system relies primarily upon eight Attitude Control Motors (ACMs) for pitch control during much of the abort trajectory in many of the likely abort scenarios. The solid-fueled ACM system consists of eight pintle-throttled nozzles connected to a common combustion chamber. The nozzles are arranged in two rings of four nozzles each around the LAV tower just aft of the nosecone. The ACMs are staggered so that there is a nozzle exit every 45° around the tower's circumference.

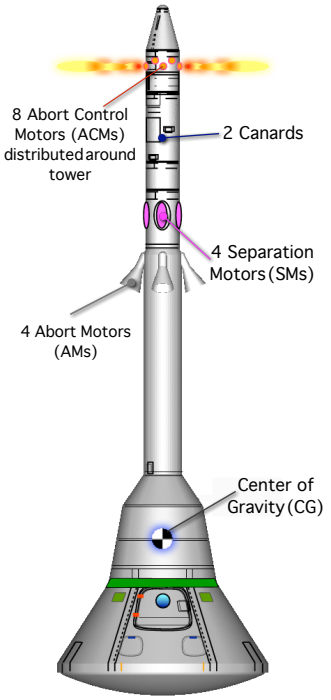

Figure 1: Schematic showing major components of the Orion LAV.

† Aerospace Engineer, NASA Advanced Supercomputing Division, Senior Member AIAA
‡ Aerospace Engineer, NASA Advanced Supercomputing Division, Associate Member AIAA

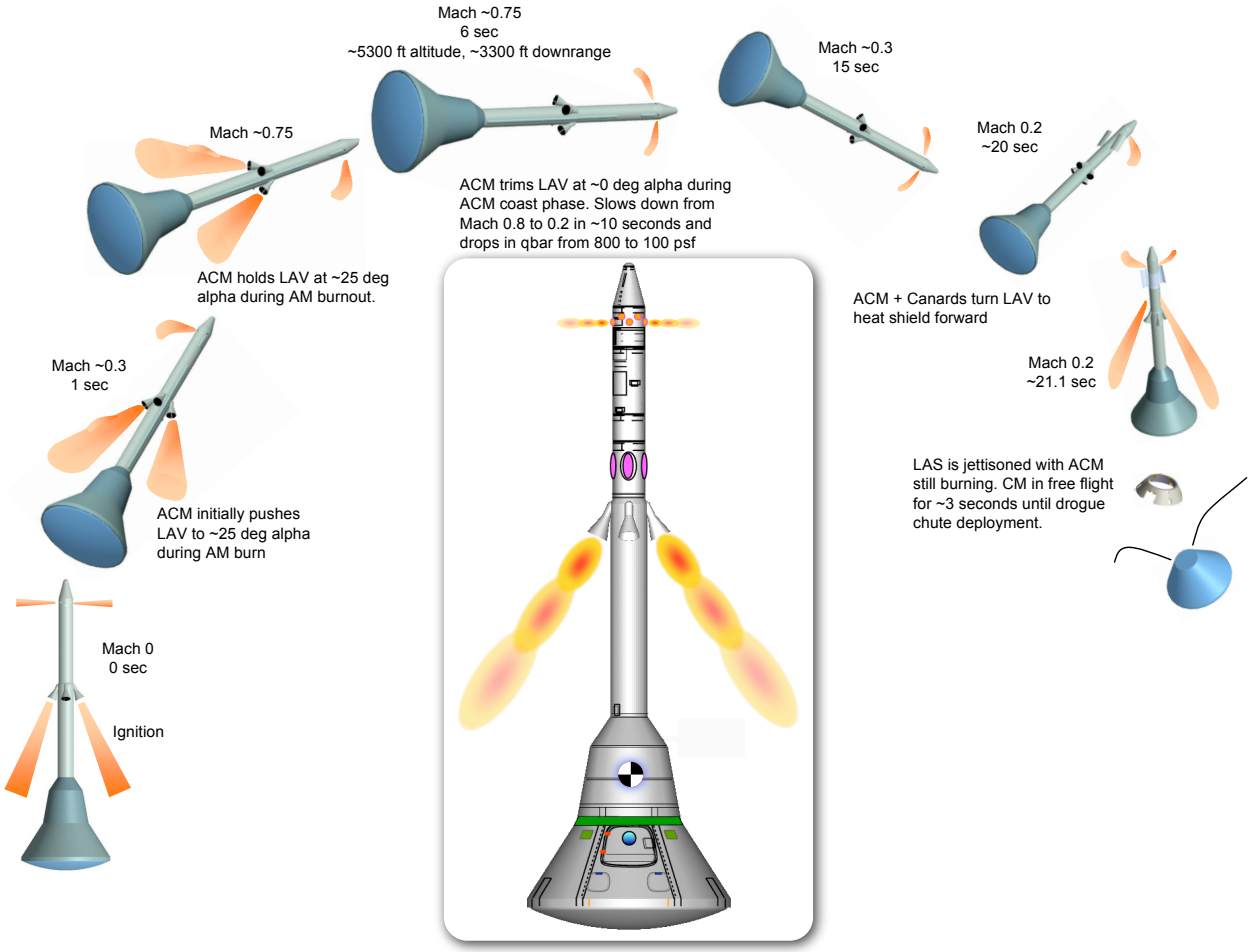

Figure 2: Schematic of abort scenario showing role of the ACM system for attitude control during AM burn and canard-assisted pitch maneuver. Timeline is approximate for an abort initiated sea level.

Figure 2 shows the major phases of one abort scenario to illustrate the critical role of the ACMs for attitude control of the LAV. The timeline in the figure is approximate for a Pad-Abort scenario initiated nominally at Mach 0. At abort initiation, the Abort Motors (AMs) ignite, pulling the LAV clear of the launch vehicle at their maximum rated thrust. Upon ignition of the AMs the ACM motor also ignites, initially generating symmetric thrust from all eight nozzles for zero net pitching moment. One second later, the LAV is traveling approximately Mach 0.3, and the ACMs reconfigure to pitch the LAV to approximately 25° angle-of-attack to begin turning the vehicle downrange. The ACMs hold this angle-of-attack while the vehicle accelerates to approximately Mach 0.75 through AM burnout. During the coast phase, the vehicle decelerates from nearly Mach 0.8 to Mach 0.3. While coasting, the ACMs continue to burn and trim the vehicle at near 0° alpha to maximize downrange distance and. Approximately 15 seconds into the abort, the canards deploy and combine with asymmetric ACM thrust to flip the vehicle over 180° to a heat-shield forward attitude. At approximately 21 seconds into the abort, with the ACMs burning in a symmetric configuration, the separation motors fire to jettison the entire launch abort system and release the Crew Module for a parachute recovery.

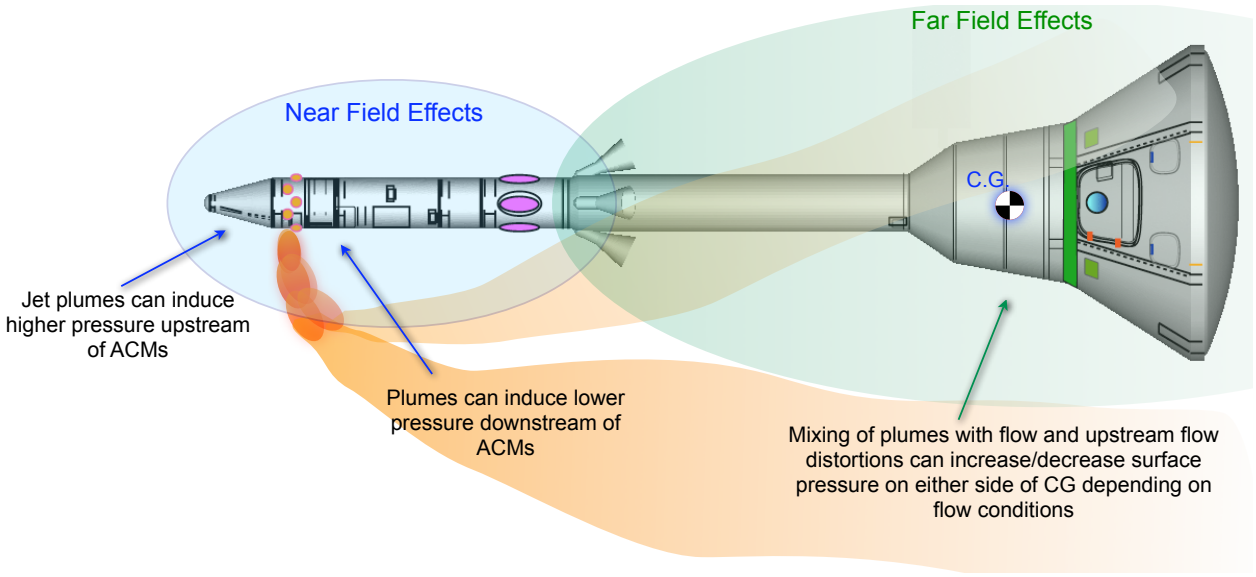

Figure 3: Schematic of some aerodynamic phenomena associated with ACM Jet Interaction.

Understanding the interaction of the ACM jets with the surrounding flow field is critical to predicting the performance and mitigating risks associated with the ACM system. Jet Interaction (JI) effects can amplify or attenuate the ACM's control authority. In certain severe cases it can actually cause a control reversal in which adverse JI overpowers the intended moment produced by the ACM jets resulting in a net pitch moment opposite that intended. Figure 3 outlines some of the more obvious JI effects. Since the oncoming flow must turn around the plumes, the cross-flow jets typically induce higher pressure upstream and lower pressure immediately downstream of the jet exits. Farther downstream the effects depend upon the jet strength, total angle-of-attack, Mach number, dynamic pressure and other variables. In the case of the LAV, with the ACMs on the tower far ahead of the center of gravity (C.G.), the near field effects have a substantial moment-arm, but act over a small surface area. In contrast, the far-field JI acting on the Boost Protective Cover (BPC) of the command module has a very small moment arm, but acts on a much larger surface area.

This paper details a series of numerical investigations undertaken to predict the control authority of the ACM and study the relevant JI. This study consisted of a large matrix of cases which were taken from the launch trajectory of a candidate LAV design. The objective of these simulations is to determine plume on/off aerodynamic increments and to populate an aero-loads database for the LAV with ACMs firing. These simulations used the geometry of a preliminary Pad Abort (PA-1) model of the LAV along with ACM nozzle exit conditions delivered by the Orion program's contractors and subcontractors. This multi-fidelity study utilized over 650 steady and unsteady inviscid simulations performed with the Cart3D simulation package[1-5] along with 53

time-dependent overset-grid Reynolds Averaged Navier-Stokes (RANS) simulations using NASA's Overflow solver.[6,9,10]

2 Solvers and Models

The work in this paper describes only a small part of the simulation effort aimed at evaluating one particular design revision in the development of the LAV for Orion. In addition to ACM studies, other analyses examine aero-performance of the Abort Motors, canards and other aspects of the vehicle. These analyses are captured in an evolving aerodynamic database which is updated as the vehicle design evolves from iteration to iteration. The scope of this database is such that tens of thousands of flight conditions and hundreds of configurations need to be analyzed. Even with access to massive supercomputing capabilities, the number of high-fidelity solutions are limited by resource and schedule constraints. Thus it is imperative that the the best data possible be produced with the least expensive approach. Thus the bulk of the current simulations were produced using an Euler solver, and a much smaller number of cases were run with a RANS solver.

2.1 Solvers

The Cart3D code is an inviscid simulation package targeted at conceptual and preliminary design of aerospace vehicles with complex geometry. The cut-cell Cartesian mesh package includes a solver module based on a second-order, cell-centered, finite-volume scheme. Upwind spatial discretization combined with a multigrid-accelerated Runge-Kutta scheme provides advance to steady-state. Unsteady simulations are performed using a dual-time method which uses the explicit multigrid algorithm as a smoother for the fully-implicit method. Parallel scalability is obtained using a domain-decomposition approach and near ideal parallel scalability has been demonstrated on systems with thousands of processors. Complete background information on Cart3D, the meshing system and implementation of the parallel solver are available in refs. [1-5].

Overflow uses a finite-difference approach and overset meshing to solve the Reynolds-Averaged Navier-Stokes equations.[6,9,10] The distributed memory build of this solver uses MPI message passing for passing inter-zonal boundary data. Load-balancing is obtained by distributing the zones among all CPUs allocated to a job. Spatial discretization used central-differencing with Roe matrix dissipation along with the Baldwin-Barth turbulence model. Cases were advanced using full-mutigrid to obtain a base solution and then run out time-dependent with the code in dual-time mode using an implicit approximate factorization scheme.

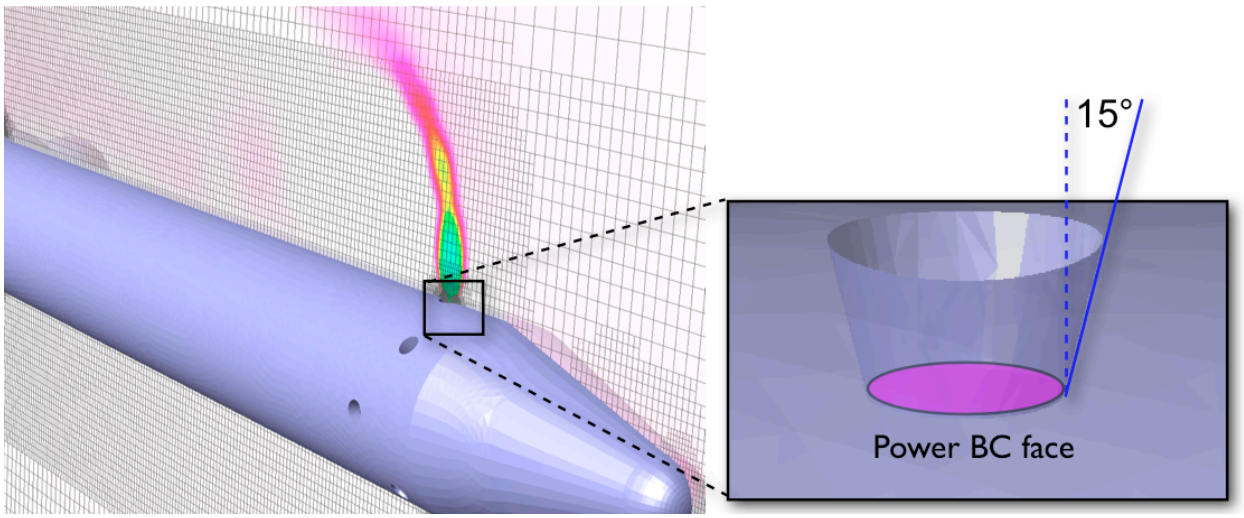

Figure 4: Detail of ACM geometry in model, power BC face is inset 2 inches from outer diameter with a 15° nozzle.

2.2 ACM Modeling

Figure 4 shows details of the geometric modeling of the ACM nozzles. The nozzles were created starting at the exit plane and integrating ACM performance data. This integrated plume exit conditions was then recessed into a beveled nozzle for application of the power boundary condition 2 inches from the outer diameter of the forebody. The nozzle walls are straight with a 15° splay. ACM exit conditions were then applied to the power-face only using 1-D isentropic relations to account for the area change. The plumes were approximated using cold-flow assumptions with a simulant gas having the same ratio of specific heats as the free-stream. In reality, the ACM nozzles are throttled using pintles to control throat area with complicated real-gas flow within the nozzles and plumes. The boundary conditions used in the present investigation matched exit Mach, exit pressure and net thrust, but are clearly idealizations of the true setup.

Figure 5 shows details of the nozzle thrust arrangement for the two power-on cases. The "5000 lbf nominal" condition has 5 active nozzles and delivers a net thrust of 5129 lbf. The "2500 lbf nominal" case has all 8 ACM nozzles active (to prevent buildup of chamber pressure) and the pintles are arranged to deliver 2513 lbf net nose-up thrust.

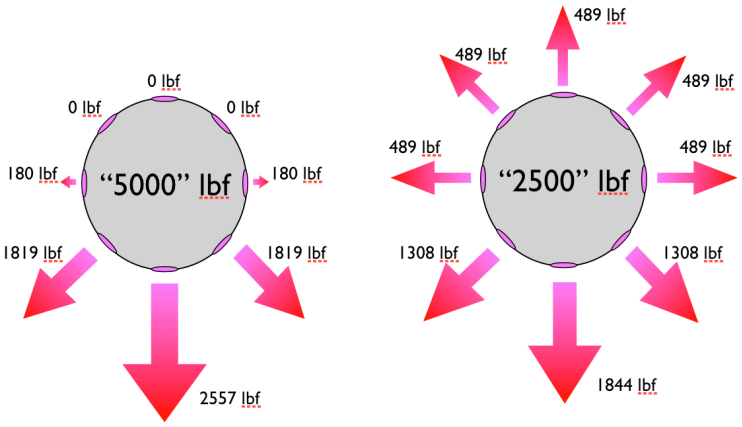

Figure 5: ACM nozzle output for the "5000 lbf" (ACM_5k) and "2500 lbf" (ACM_2.5k) thrust settings. The "5000 lbf nominal" setting delivers to 5129 lbf actual thrust. The "2500 lbf nominal" setting delivers 2513 lbf actual.

2.3 Simulation Matrix

The simulation matrix was drawn from both the pad-abort and vehicle launch scenarios, and included a baseline (*ACM_off*) and two powered ACM settings. ACM thrust in the plume-on cases was arranged to produce a nose-up pitch moment with 2500lbf (*ACM_2.5k*) and 5000lbf (*ACM_5k*) net thrust coming from the combined efforts of the 8 ACM nozzles. Inviscid cases were run at 13 angles-of-attack in the range $\alpha = \{-30° - 50°\}$ and for 11 Mach numbers, $M_\infty = \{0.3, 0.5, 0.7, 0.91, 1.11, 1.32, 1.63, 2.03, 3.0, 4.0, 6.02\}$, spanning subsonic to mid-supersonic flow regimes. Inviscid cases were also computed at sideslip angles of $\beta = \{0° \& 30°\}$. RANS cases were run with the same ACM thrust settings but over a more restricted range of Mach numbers, $M_\infty = \{0.3, 0.5, 0.7, 1.3\}$ and $\alpha = \{-10° - 30°\}$. RANS cases for ACM_2.5k were run only at $M_\infty = 0.7$, and none of the RANS cases considered sideslip ($\beta = 0°$). Figure 6 shows the variation of Mach and Reynolds numbers along the nominal trajectory studied in the simulation matrix. Both inviscid and RANS solvers use free-stream quantities to normalize the dependent variables in the simulation. Since chamber conditions for the ACMs are essentially invariant with altitude, the power settings in §2.2 must be rescaled by the free-stream normalization to account for altitude at various points along the trajectory.

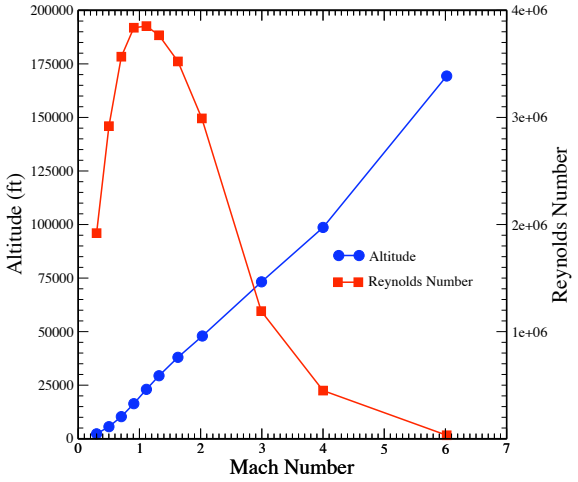

Figure 6: Variation of Mach and Reynolds numbers along nominal LAV trajectory considered in the simulation matrix.

3 Geometry and Mesh Generation

Simulations were performed on the official release of the LAV CAD geometry. This model of the vehicle geometry was accessed directly through the CAPRI interface to obtain a watertight trian-

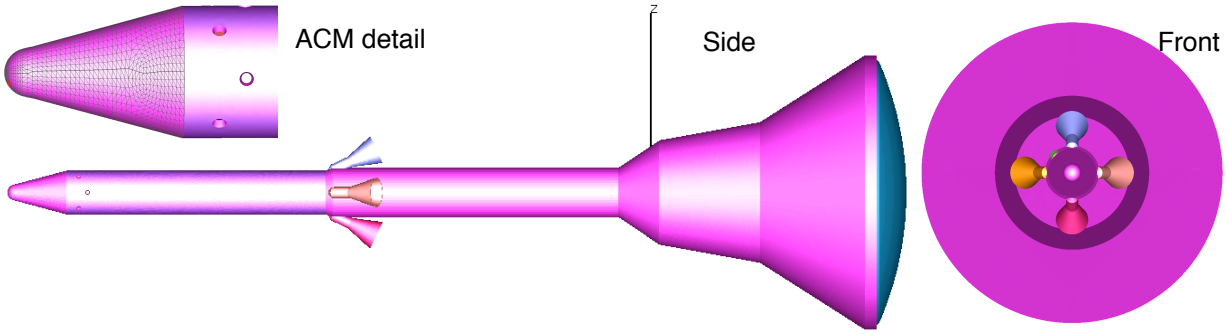

Figure 7: Views of computational model of LAV with 23 components and ~380,000 triangles. ACM nozzles are conical with 15° splay.

gulation of the wetted surface using the triangulation techniques outlined in Ref. [7]. Figure 7 shows several views of the wetted surface through a rendering of this triangulation. In total, this description contained approximately 380k triangles and was used directly by the meshing module in Cart3D. It includes 24 components including ACMs, AMs, the LAV tower, command module, BPC and heatshield. This same triangulation of the LAV was used as an underlying geometry description for structured overset meshing using the Chimera Grid Tools package.[11,12] Figure 7 shows details of the triangulation and ACM nozzles near the nose. Notably, this revision of the LAV has the Abort Motors (AMs) in the "plus" orientation, and has the ACMs staggered in two circumferential rings. The aft ring of ACMs is oriented in the principle compass directions, and the forward ring is staggered 45° in an "**x**" orientation.

3.1 Overset Mesh

The Chimera Grid Tools software[11,12] was used to develop an overset grid system via an automated script system which embedded conformal near-body grids in background Cartesian blocks. This process generated structured surface and volume grids and performed the necessary hole-cutting using Pegasus5[13]. The same version of the entire grid system was used for all cases in this analysis. Near the ACMs, grids included a cylindrical, off-body volume grids intended to resolve the near-body region of the ACM plumes. In total, the grid system contained 44 zones and 21.9 million grid points. Figure 8 shows several images of the grids. The top frame contains a view showing the vertical symmetry plane, while the middle frame shows a close-up of the surface grids in the vicinity of the ACMs. Annular ACM nozzle grids splay onto the outer diameter of the LAV tower. A cross-section of an

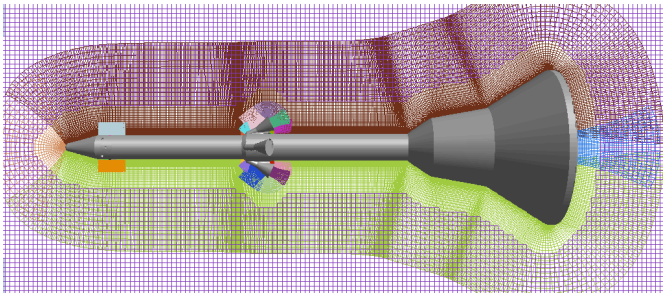

Image of the grid slices in the Y=0 plane.

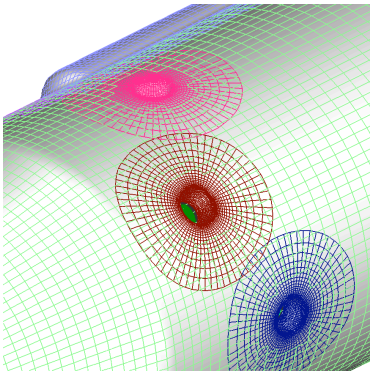

Close-up view of the surface grids in the vicinity of the ACM nozzles.

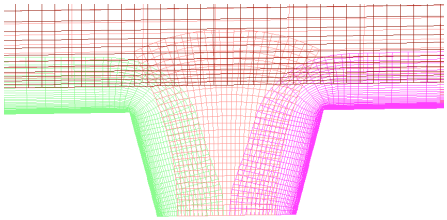

Cross-section view the grids inside one of the ACM nozzles.

Figure 8: Selected views of the Overset mesh used for simulations with Overflow. 21.9M grid points.

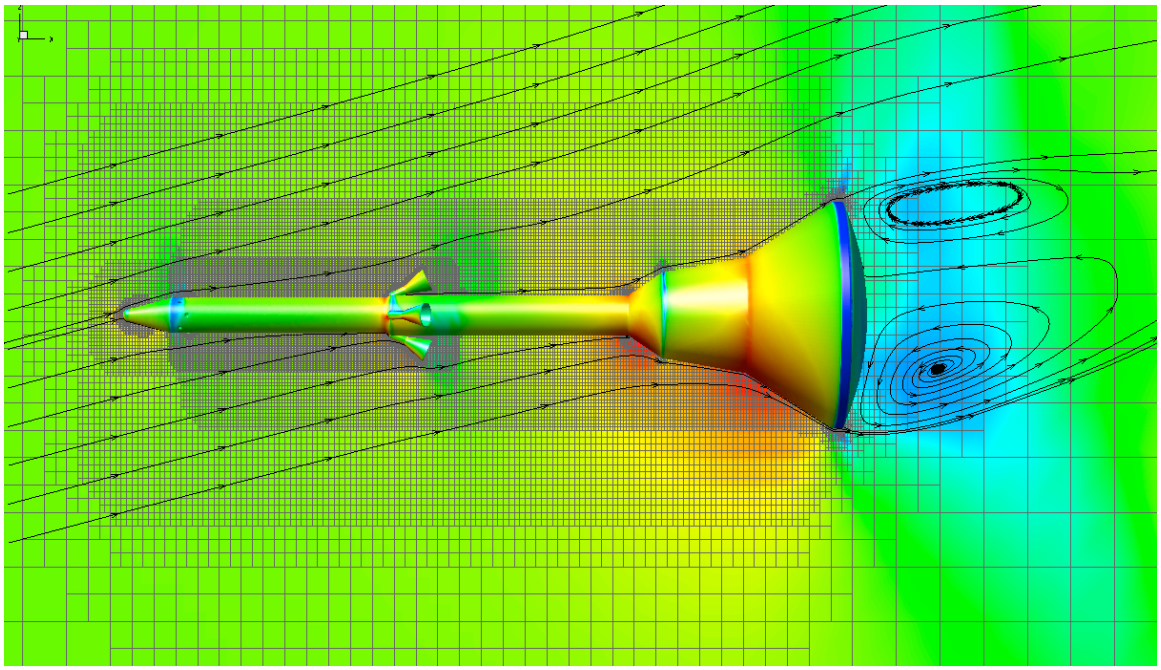

Figure 9: Pitch-plane (*X-Z*) slice through standard Cartesian mesh used for inviscid steady-state simulations. Mesh has 4.9M cells, with 520k cells intersecting the surface of the geometry.

individual ACM nozzle is shown in the lower frame of Figure 8. Within each ACM, an annular grid follows the geometry surface out of the nozzle while a second overlapping grid resolves the core of the nozzle.

3.2 Baseline Cartesian Mesh

Inviscid simulations were performed using a cut-cell Cartesian mesh automatically generated by the Cart3D simulation package. Figure 9 shows a pitch-plane cut through the baseline Cartesian mesh used for the steady inviscid simulations. This mesh had about 4.9 million cells in total, with roughly 520 thousand cells intersecting the surface of the geometry. This mesh is actually the end result of grid refinement studies that have been conducted over the course of analyzing three similar LAV configurations. Refinement studies were carried out at sub/trans/supersonic Mach numbers and at several incidence angles. To manage complexity and reduce risk, the same mesh was used at all Mach numbers and all angles-of-attack. This is an obvious compromise since the important flow structures change radically with speed regime and flow incidence. Additionally, refinement studies conducted at subsonic through low-supersonic Mach numbers indicated moderate to severe unsteadiness in the vehicle's wake and behind the inactive nozzles of the separation motors. As a result, a main challenge in meshing this geometry for steady-state simulation is to choose a mesh that is fine-enough to produce reasonable force and moment coefficients, but not so fine that unsteadiness in the simulation makes steady-state tools inadequate.

Our investigations focused on accurately and economically predicting integrated force and moment data over a wide range of cases. In this study, the accuracy of a particular simulation depends upon both the resolution of sensitive regions flow field, and the net impact of these regions on the integrated force/moment data. Since flow sensitivity varies both with speed-regime and flow incidence, a mesh with fixed resolution will obviously produce data whose uncertainty varies on a case-by-case basis. The goal of the mesh refinement studies was to mitigate this uncertainty by producing a mesh which yielded mesh-converged force and moment data over as large a portion of the run matrix as was economically feasible. The final mesh has relatively high resolution surrounding the upstream-facing portions of the geometry, but coarsens rapidly at the shoulder of the heat shield.

3.3 Unsteady Inviscid Mesh

The mesh refinement and flow field sensitivity investigations showed that the standard mesh (Fig. 9) produced essentially mesh converged results over a broad range of sub-, trans-, and supersonic flight conditions. Mesh convergence at supersonic conditions (above Mach 1.6) was very good for all coefficients. Below about Mach 1.6, mesh convergence of normal force, side force, pitching moment and yawing moment remained quite good, however axial force continued to display sensitivity to mesh.

At sub- and transonic conditions, sensitivity analysis showed a strong relationship between axial force and discretization errors due to mesh coarseness near the Command Module (CM) shoulder

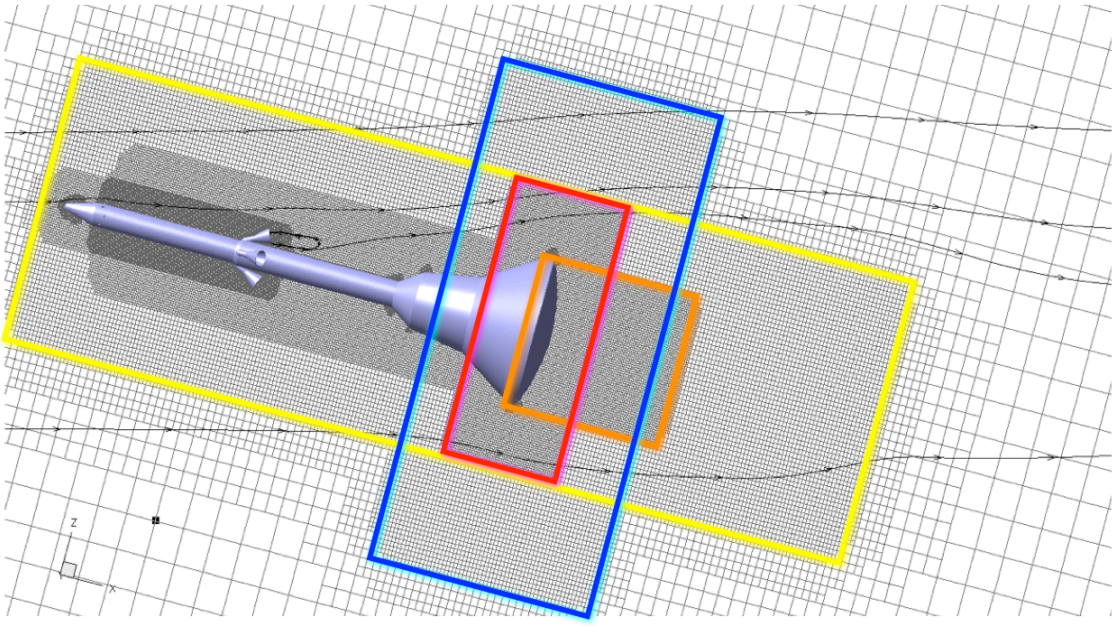

Figure 10: Pitch-plane slice through Cartesian mesh used for unsteady flow simulations with overlay of prespecified refinement regions. This mesh is based upon the standard mesh used in the steady simulations (Fig. 9) with the addition of the 4 additional off-body mesh refinement regions shown.

and wake region. In the mesh refinement studies, increasing resolution in these areas was found to trigger substantial flow field unsteadiness, hampering convergence of steady-state simulations. Conversely, using coarser grids near the CM shoulder and wake regions suppressed this unsteadiness through the greater dissipation associated with the use of larger cells. The mesh studies indicated that contamination due to this increased dissipation was primarily confined to the axial force integration, and that other functionals were less sensitive. This observation is not surprising since errors in this region of the flow are transmitted to the surface through the heatshield which is symmetric about the *x*-axis and projects mainly in the axial direction.

To adequately resolve the flow field near the CM shoulder and in the wake region roughly two million cells were added through additional pre-specified adaptation regions. This produced a mesh with roughly 6.8 million cells, about 540,000 of which intersect the surface. Figure 10 shows an image of this mesh via a pitch-plane (*X*-*Z*) slice through the mesh. Overlaid on the mesh are the outlines of the additional pre-specified adaptation regions that were added to enhance off-body resolution near the CM shoulder and wake. This mesh was used for all unsteady simulations.

4 Simulation Details

Our study of ACM effectiveness used a multi-fidelity approach. Steady-state inviscid runs were performed covering the entire simulation matrix. As described in the next section, aerodynamic data from these runs were fortified with axial-force corrections which are generated using unsteady runs with the same inviscid solver (Cart3D). RANS simulations (Overflow) provided both spot-checks for the corrected inviscid data and were used to develop viscous increments to the inviscid simulation data. In addition, trend information in the most critical cases was double-checked by covering certain portions of the Mach-alpha space with both inviscid and viscous simulation tools.

References [6] and [14] give full details of the code settings, convergence criteria and force, moment and residual histories for the RANS and inviscid simulations over the entire simulation matrix. In this section we briefly highlight the development of the unsteady axial-force correction applied to the steady inviscid results to demonstrate the efficacy of the approach

4.1 Unsteady Base-Correction

Unsteady inviscid simulations were performed using Cart3D on a small subset of the simulation matrix using the mesh in Figure 10. In total, 16 unsteady cases were computed for the LAV without power (ACM_off only) at M_∞ = {0.3, 0.5, 0.7, 0.91, 1.11, 1.32, 1.63, 2.03} and two incidence

angles α = {0°, 50°}. These simulations used 4-level multigrid as an inner smoother for the second-order backward time integration as detailed in reference [14]. The primary result of these simulations were time-averaged force coefficients.

Figure 11 shows a typical example from this collection of unsteady runs. The figure contains two solution snapshots and force coefficient time histories from a simulation at Mach 0.7, alpha = 15° (ACM_off). The solution snapshots were taken at non-dimensional times of t = 28000 and t = 32000. These illustrate substantial unsteadiness in the bluff-body wake while the solution upstream of the heat shield remains relatively static. The time-histories of the axial-force coefficient (C_A), side-force coefficient (C_Y), and the normal-force coefficient (C_N) are displayed in the figure, and are typical of those observed in all the unsteady run cases. Time-averaged coefficients for this case were computed from t = 7480 until the end of the run at t = 34280. The time averaged values of C_A and C_N are 0.562 and 0.281, respectively.

The primary difference between the steady-state and the time-averaged unsteady force coefficients is the axial force; the other force are nearly identical between the two ap-

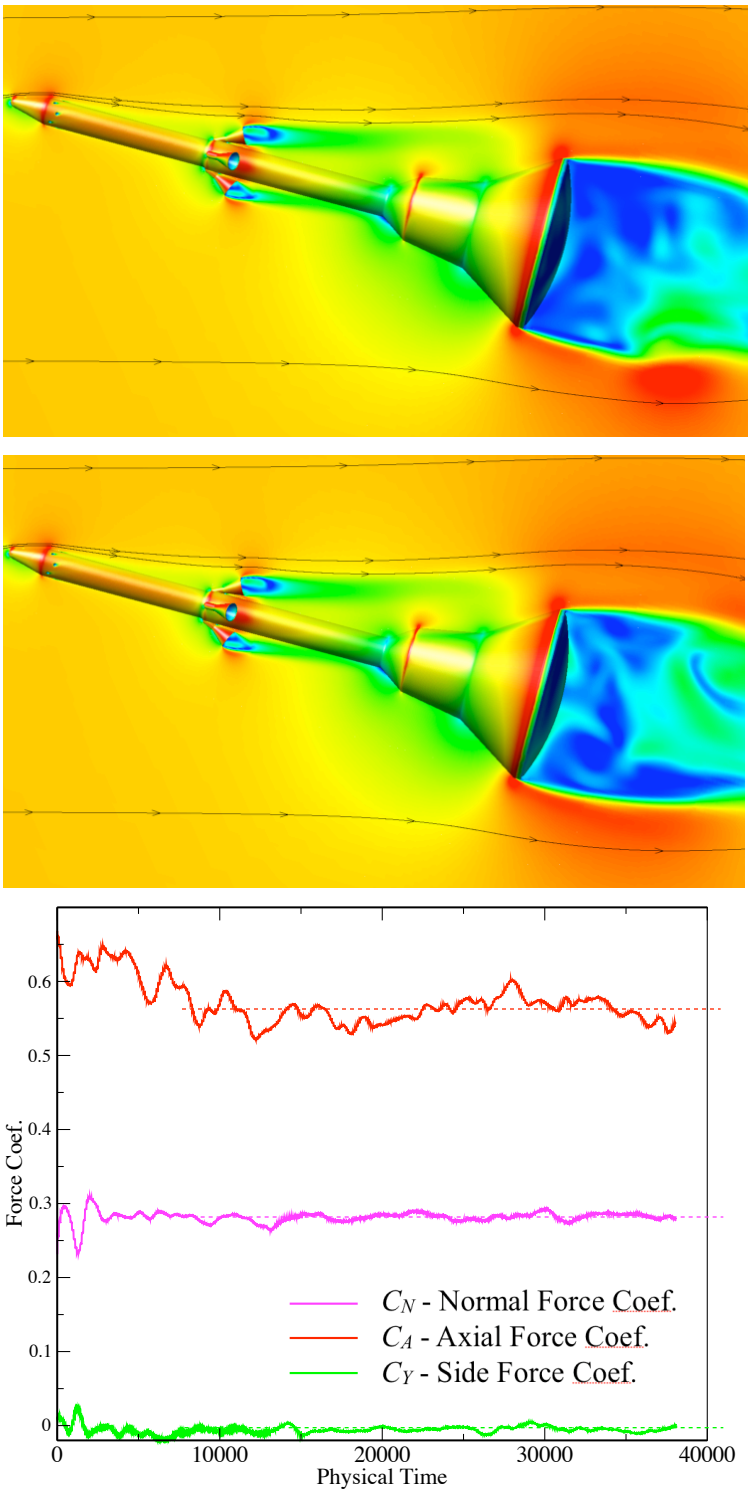

Figure 11: Solution mach contours and unsteady time-history of force coefficients for ACM-off case at Mach 0.7 α = 15°. Mach contours shown at two time levels: in the upper frame, time = 28000, in the lower frame, time = 32000. Time averaging for this case started at t = 7480.

proaches. With increased resolution around the command module shoulder, the bluff wake the unsteady calculations tends to separate sooner, the flow expands less, and the back pressure acting on the heat shield is slightly higher. When integrated over the entire heat shield, this results in a lower axial force for the unsteady simulations. This difference is most pronounced at the lower Mach number cases and essentially vanishes at free-stream Mach numbers greater than two. At all Mach numbers, the forces acting on the vehicle forward of the CM shoulder are nearly identical in the steady-state and unsteady simulations.

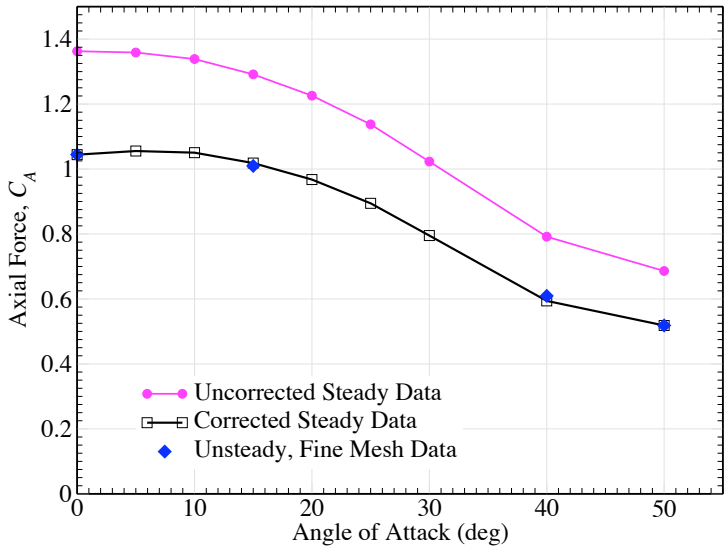

Figure 12: Variation of Axial force (C_A) data with angle-of-attack at Mach 1.32 comparing steady-state simulations (pink circles), unsteady simulations (solid blue diamonds), and base-corrected steady simulations (open black squares).

These unsteady simulations were used to develop a correction to the steady-state C_A as a function of the angle of attack was developed and is of the form:

$$C_{A_{Corrected}}(\alpha) = C_{A_{Steady}} + (1-f)\Delta_{0^o} + f\Delta_{50^o} \quad (1)$$

where

$$f = \frac{|\alpha|}{50^\circ} \quad (2)$$

and

$$\Delta_\alpha = (C_{A_{Unsteady}})_\alpha - (C_{A_{Steady}})_\alpha \quad (3)$$

The unsteady runs were used to develop unsteady corrections each Mach number in the unsteady inviscid case matrix. Figure 12 plots the axial-force data versus angle of attack for Mach = 1.32. In this figure, the solid blue diamond symbols indicate time-averages of the unsteady simulations, the solid pink circles show the steady-state results on the baseline mesh, and the black squares show the corrected steady-state results. Since the corrected data is anchored at 0° and 50° angle-of-attack, the corrected and unsteady data are identical at these angles. The corrected data at the intermediate angles of 15° and 40° show very good agreement with the time-averaged unsteady data, giving confidence that this linear correction factor provides good agreement across the other angles-of-attack of current interest.

5 Simulation Results

5.1 Forces and Moments

Figures 13, 14 and 15 contain force and moment comparisons between the inviscid Cart3D simulations and the viscous RANS simulations from Overflow at all Mach numbers for which viscous cases were run. Along with the plots presented here, extensive comparison data exists in Ref. [7] and [14]. In the se figures Overflow simulation data is shown using open symbols while the inviscid simulation results are presented using lines. Axial forces shown in the figures includes the correction developed in the previous section (§4.1). Figure 13 shows comparison of normal force, axial force and pitching moment (C_A, C_N, & C_M) for ACM_off. Agreement is very good agreement between the two codes. Figures 14 and 15 examine the comparison with the ACMs burning at ACM_2.5k and ACM_5k settings. Data in these plots includes the contribution of the ACM jets. For the 2500lbf power level, viscous-simulation data is only available at Mach 0.7. In all three figures the comparison of axial force data between the full RANS simulations and the base-corrected inviscid data is quite good.

The inviscid simulations provided an aero-database spanning Mach numbers from 0.3 to 6.0, alpha from -30° to 50° and sideslip angles of 0° and 30° for all three ACM settings. Figure 16 presents a slice through this four-dimensional dataset through carpet plots of C_A, C_N, and C_M as functions of Mach and

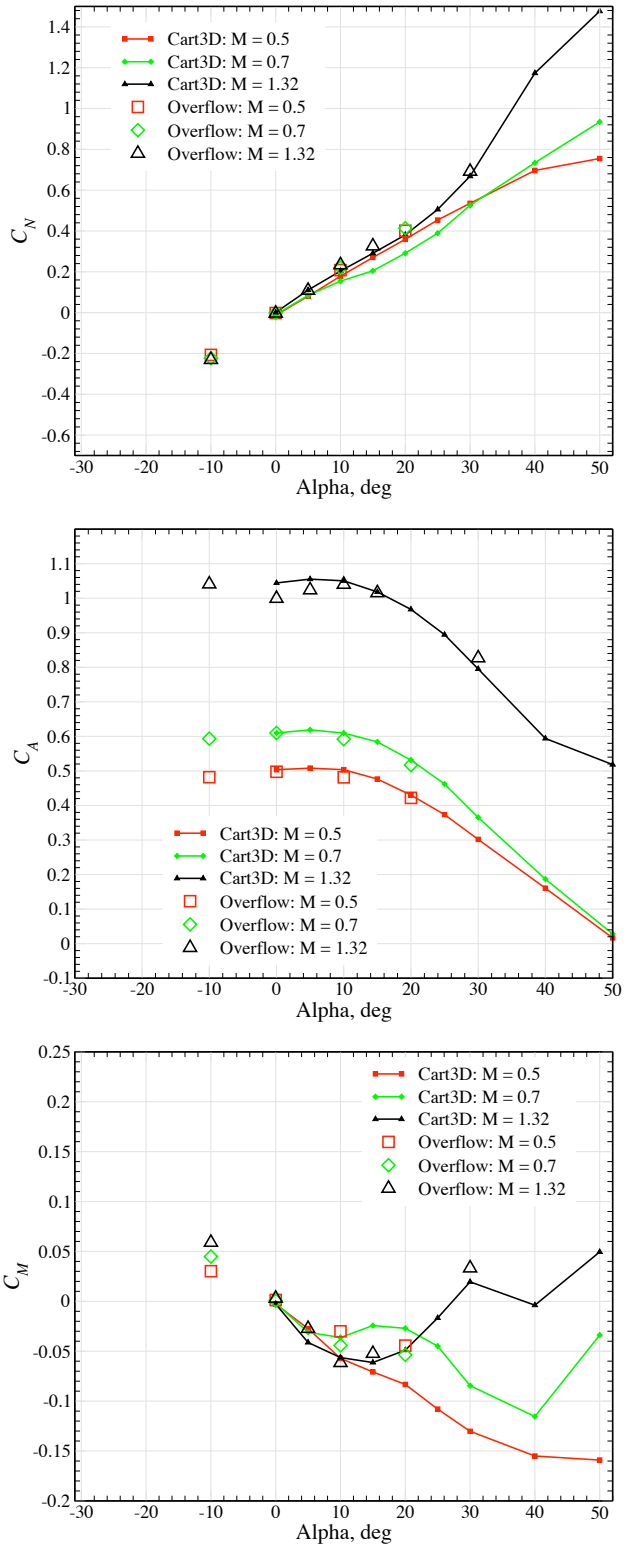

Figure 13: Axial force, normal force and pitching moment variation with angle-of-attack. ACM_off, Comparison of inviscid simulations with data from unsteady Overflow (RANS) simulations at $M_\infty = 0.5$, $M_\infty = 0.7$ & $M_\infty = 1.3$.

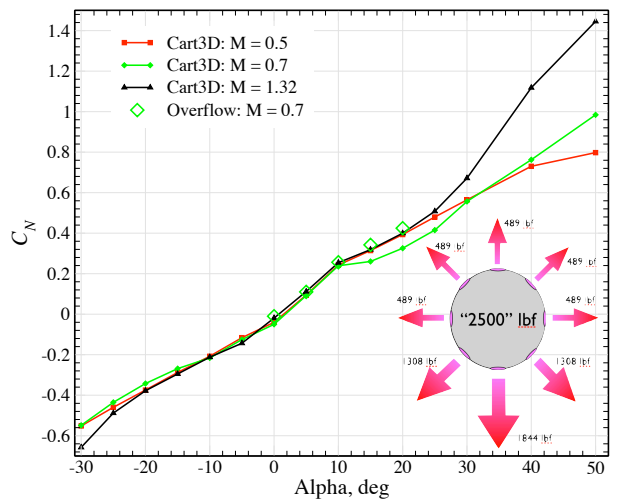

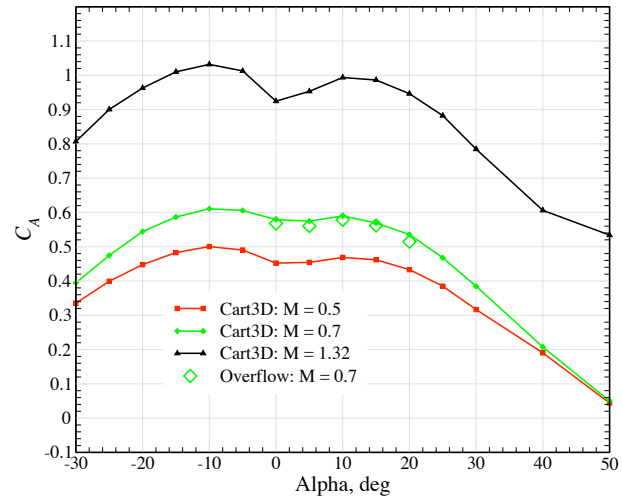

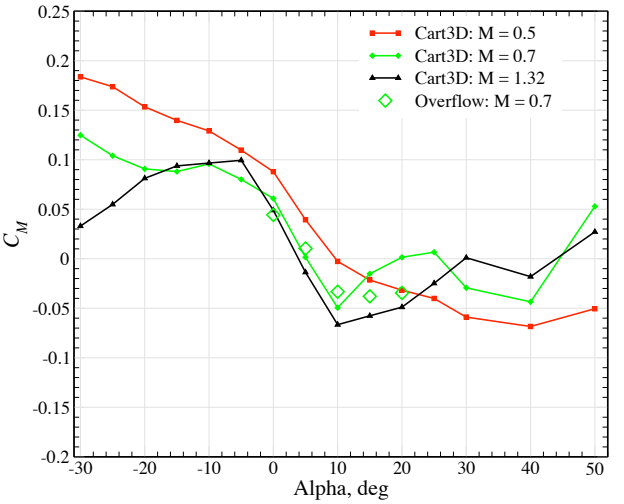

Figure 14: Normal force, axial force and pitching moment variation with angle-of-attack. ACM_2.5k, Comparison of inviscid simulations with data from unsteady Overflow (RANS) simulations at $M_\infty = 0.7$.

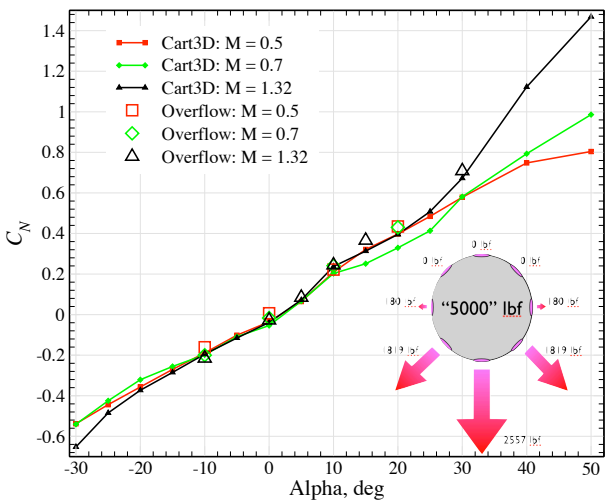

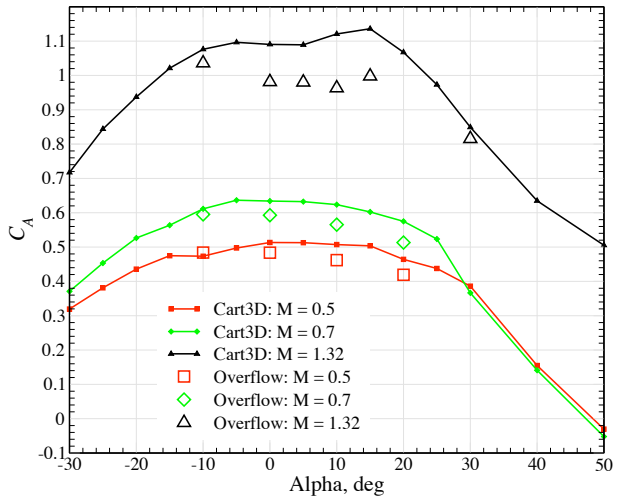

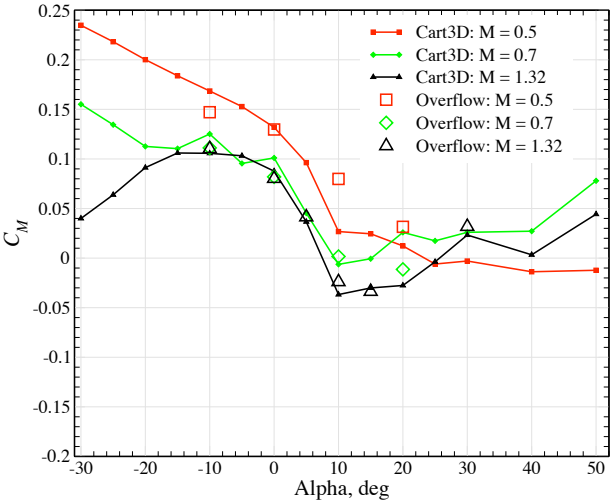

Figure 15: Axial force, normal force and pitching moment variation with angle-of-attack. ACM_5k, Comparison of inviscid simulations with data from unsteady Overflow (RANS) simulations at $M_\infty = 0.5$, $M_\infty = 0.7$, $M_\infty = 1.3$.

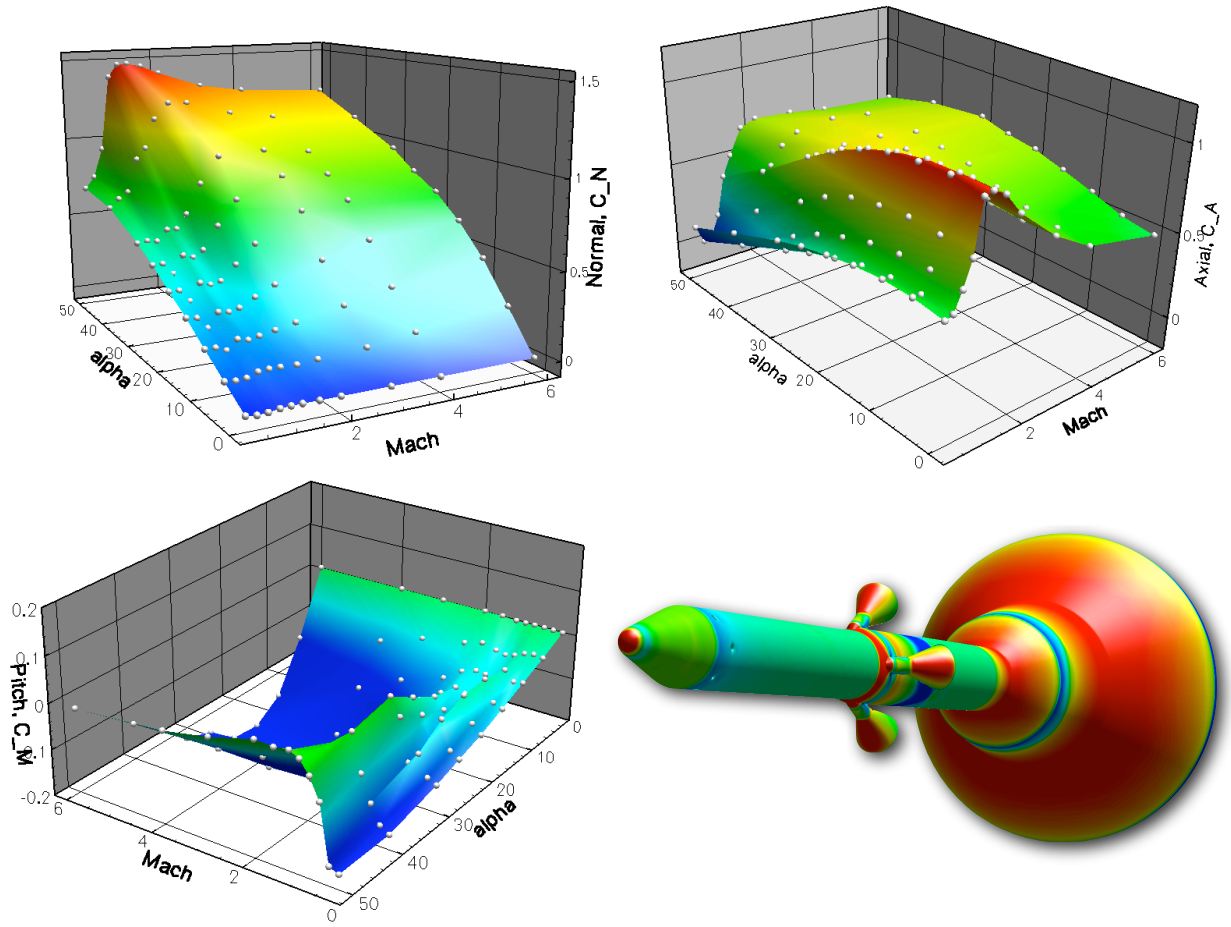

Figure 16: Carpet plots of normal force, axial force and pitching moment variation with angle-of-attack and Mach number for preliminary LAV design with ACMs off. Carpets extracted β = 0°.

angle-of-attack at β = 0° with ACM_off. The data shows relatively mild behavior at supersonic Mach numbers with more non-linear variation as the configuration passes through $M_\infty = 1$. The carpet plot of axial force shows the expected transonic drag rise and the corresponding C_m's display radical pitch variation through sonic conditions. Beyond Mach 1, the axial coefficient drops off as the shocks lay back in the accelerating flow in accordance with gas dynamic theory.

5.2 Pitching Moment Effectiveness

One objective of this investigation was to examine the pitch authority offered by the ACMs and to develop an understanding of the physics governing the ACM JI over the LAV's flight envelope. Interaction of these jets with the surrounding flow can decrease or amplify the ability of the ACMs to produce a desired pitching moment. The ACM jet pitching moment effectiveness, Eff_{Cm}, is defined as:

$$Eff_{Cm} = 1 - \frac{JI}{JT} \tag{4}$$

$$\text{with} \qquad JT = Cm_{\text{total\_no\_thrust}} - Cm_{\text{total}} \tag{5}$$

$$\text{and} \qquad JI = Cm_{\text{total\_no\_thrust}} - Cm_{\text{ACM\_off}} \tag{6}$$

Here Cm_{total} is the pitching moment on the entire LAV with ACM jets firing and $Cm_{\text{total\_no\_thrust}}$ is the integrated pitching moment on the LAV without the ACM thrust components included in the integration. Since JT is the difference between these two, it isolates the contribution of the ACMs to the LAV pitching moment. The quantity JI is the difference between $Cm_{\text{total\_no\_thrust}}$ and the integrated vehicle Cm with the ACM's turned off at the same flight condition, it is therefore the pitching moment increment due to jet-induced pressure differences over the rest of the acreage of the LAV skin. In lay terms, Eff_{Cm} can be thought of as an amplification factor of the ACM's control due to the effects of the jets on the surrounding flow. If the JI effects are zero, $Eff_{Cm} = 1$; if JI exactly cancels JT, $Eff_{Cm} = 0$. Negative values of Eff_{Cm} indicate a control reversal.

Figures 17 and 18 show ACM jet effectiveness for the ACM_2.5k and ACM_5k cases (respectively). Both plots show only minor JI effects at low Mach numbers. However from Mach 0.7 to

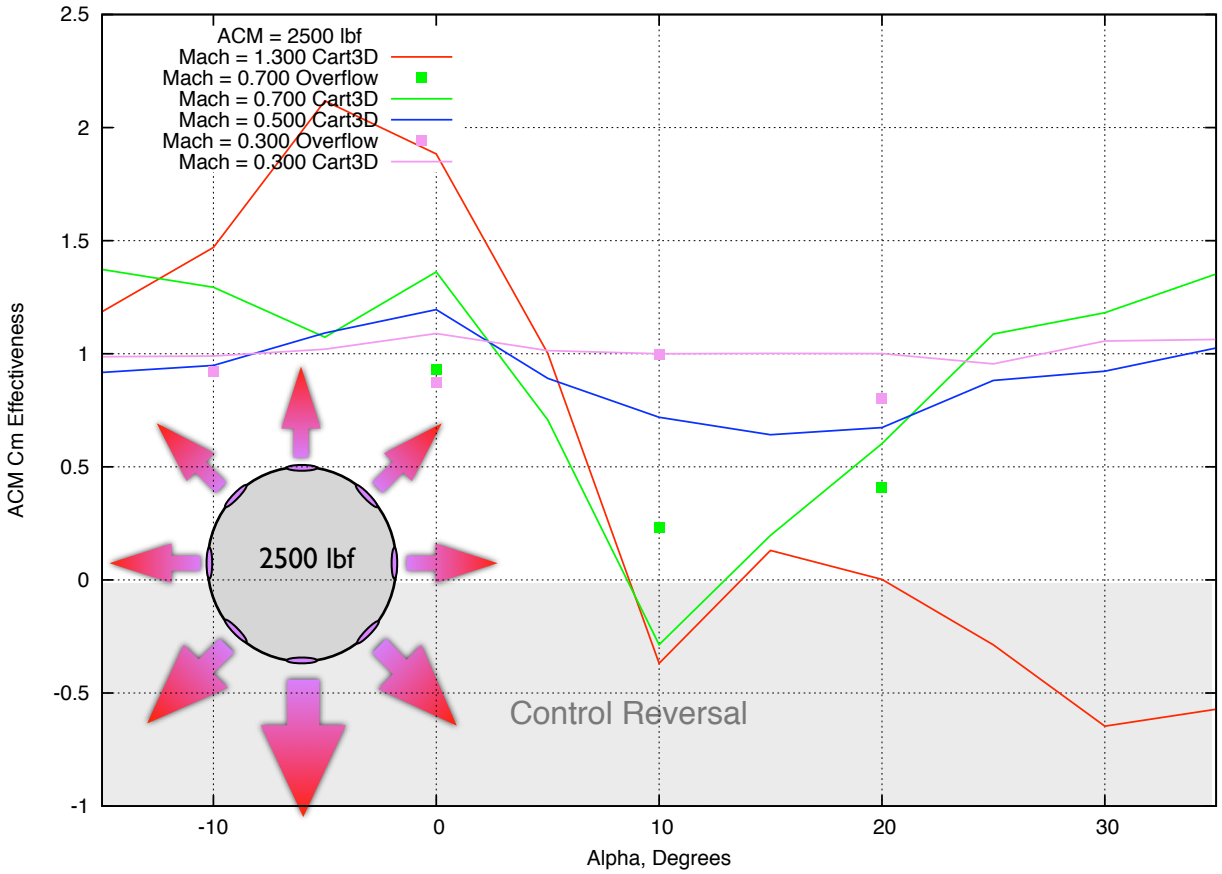

Figure 17: Variation of ACM jet pitching moment effectiveness Eff_{Cm} as a function of angle-of-attack for the ACM_2.5k cases with 2500 lbf of nominal ACM thrust.

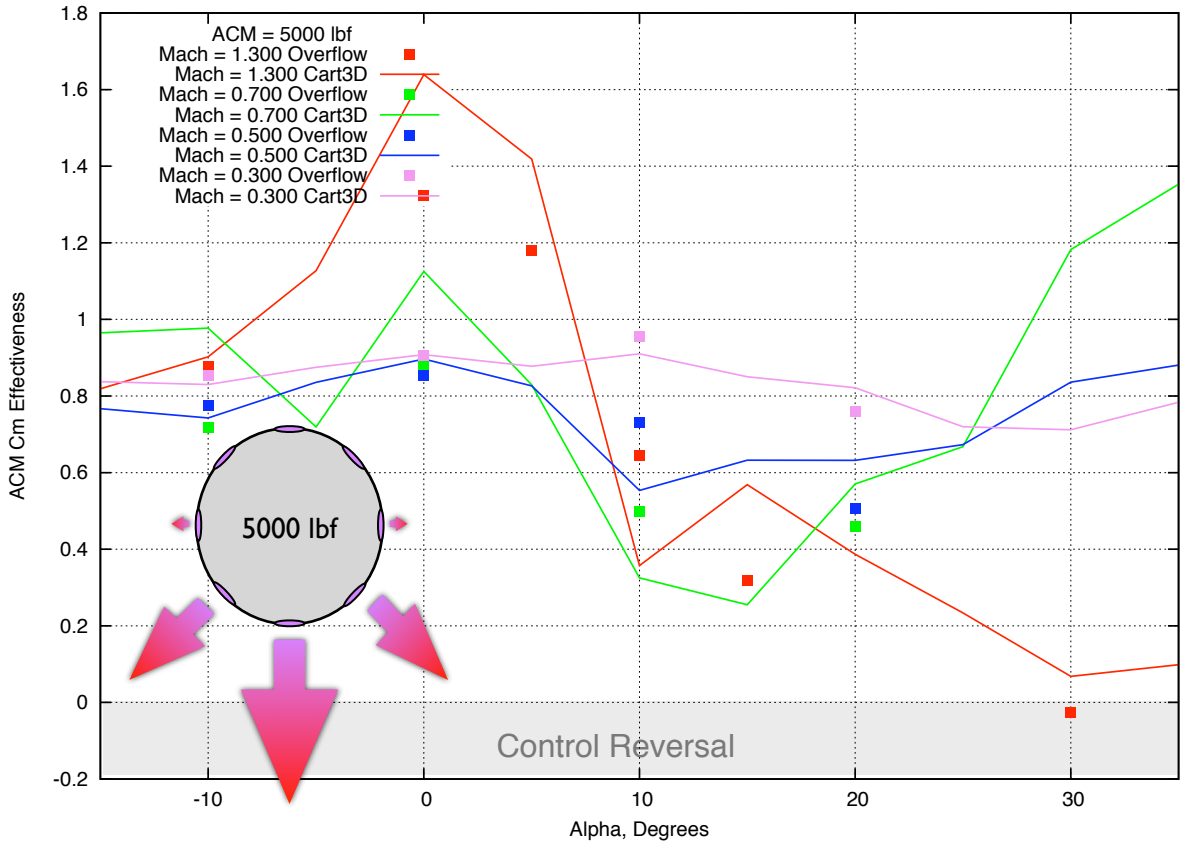

Figure 18: Variation of ACM jet pitching moment effectiveness Eff_{Cm} as a function of angle-of-attack for the ACM_5k cases with 5000 lbf of nominal ACM thrust.

Mach 1.32 there is a marked decrease in the ACM jet effectiveness with positive alpha. This adverse JI is most severe at Mach 1.32 and was predicted by both inviscid and viscous simulations. The ACM_2.5k cases show more severe JI than the ACM_5k indicating that the increased thrust profile offers more pitch authority but still suffers from severe adverse JI.

To better understand the physical mechanisms behind the complex JI effects, Figures 19-32 are composite images from the inviscid results comparing corresponding flight conditions with ACM_off to ACM_2.5k and ACM_5k. While these comparisons exist for the entire trajectory, images are only presented for selected cases to illustrate relevant physical mechanisms in the flow. In each figure, ACM_off appears above the corresponding ACM_2.5k or ACM_5k case. On the left, symmetry plane and surface contour plots of Mach number give an indication of the flow. On the right, surface pressure coefficients display the load distribution. Delta *Cp* on the surface is shown in between the ACM_off and ACM_on cases. These images were made by directly differencing local surface pressures ($\Delta Cp = Cp_{ACM\_on} - Cp_{ACM\_off}$). Red indicates over-pressure, blue indicates under-pressure, white indicates no difference.

The ΔCp plots in this series of figures (19-32) illustrates the source of the loss in ACM effectiveness at positive angle-of-attack through trans- and low supersonic Mach number flow conditions. Relative to the flow with no ACM jets, there is a low-pressure region on the surface immediately downstream of all the ACM jets. Compounding this is the "screening" effect of the strong down-firing ACM jets. These jets screen the LAV tower forebody from the oncoming flow. At high angle-of-attack and without jets firing, the free-stream impinges on the forebody producing a nose-up pitching moment. When the ACMs fire, the LAV tower downstream of the jets does not see the oncoming flow since it is "screened" by the strong down-firing ACM jet. The net effect is that the forebody acreage produces less nose-up pitching moment when compared to the case with ACM off. At Mach 1.32 and $\alpha = 25°$ Figures 25 and 26 clearly illustrate this situation.

Figures 33-40 show composite images with comparisons of simulations performed using both Cart3D and Overflow. These images show Mach contours and surface pressure coefficients and the examples include ACM_off, ACM_2.5k and ACM_5k. Each of these comparison figures contains symmetry-plane Mach contours on the left and surface pressure coefficient on the right. Although data is only available over a portion of the full run matrix, these comparisons illustrate the differences between the inviscid simulations and the results of full RANS simulations. In general these show that while the the steady inviscid modeling in the Cart3D simulations is deficient near the surface and in wakes, it does capture the majority of the complex off-body flow features and generally predict accurate detailed pressure loading on the LAV. An expanded set of comparison figures are contained in Refs. [6] and [14].

All of these cases were run on NASA's Columbia supercomputer system.[15] This system is actually a supercluster of SGI Altix nodes with 512 Itanium2 processors each and shared-memory within each node. Each steady-state Cart3D simulation required 10-20 CPU-hours on this system while the unsteady inviscid simulations used about 10 times that. Each RANS simulation required on the order of 1000 CPU hours. Reference [15] contains a detailed look at the performance of each of these simulation tools on this particular system.

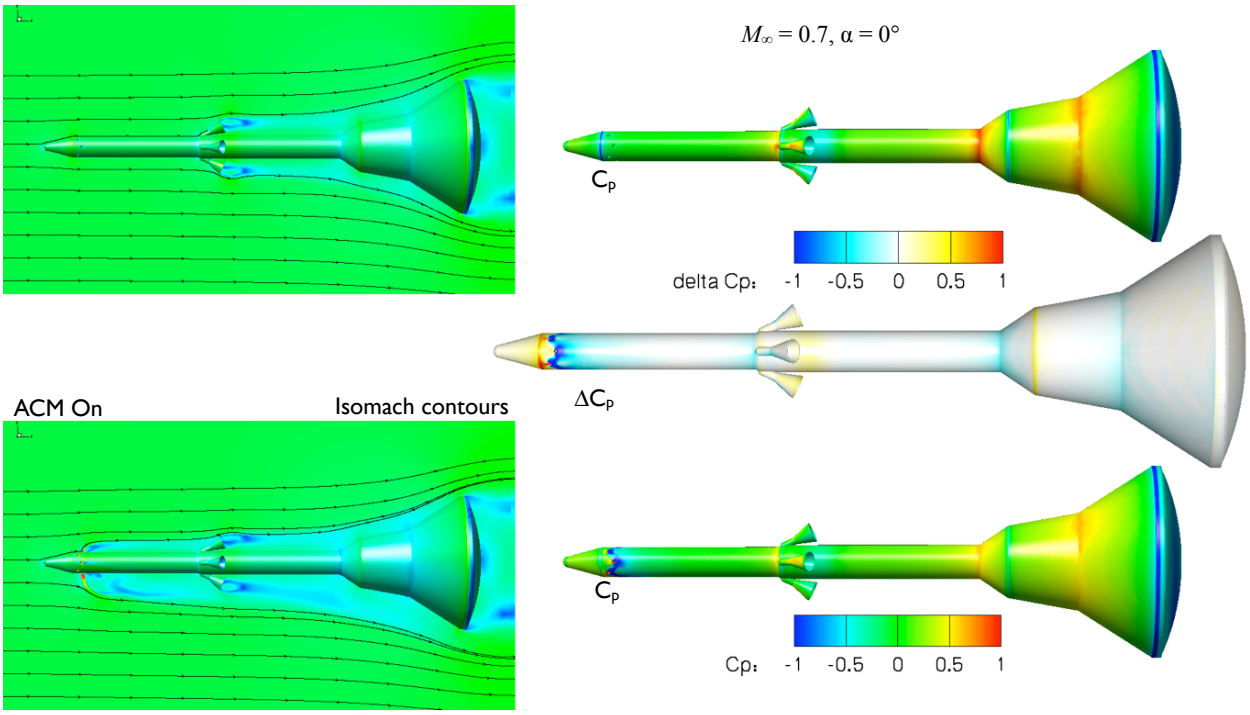

Figure 19: Flow field and load comparison with (lower) and without (upper) ACM jets. Symmetry-plane isomach contours (left), and surface *Cp* contours (right). Delta *Cp* (middle right) is $\Delta Cp = Cp_{ACM\_on} - Cp_{ACM\_off}$. ACM_2.5k, $M_\infty = 0.7$, $\alpha = 0°$.

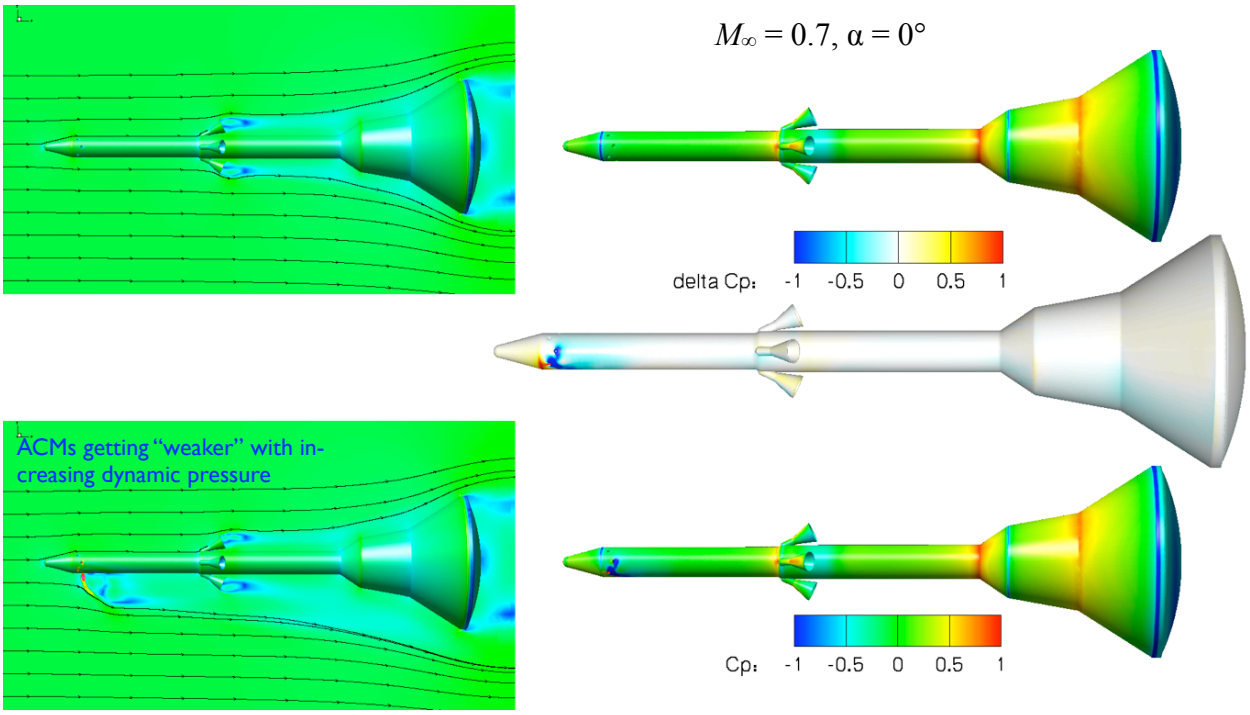

Figure 20: Flow field and load comparison with (lower) and without (upper) ACM jets. Symmetry-plane isomach contours (left), and surface *Cp* contours (right). Delta *Cp* (middle right) is $\Delta Cp = Cp_{ACM\_on} - Cp_{ACM\_off}$. ACM_5k, $M_\infty = 0.7$, $\alpha = 0°$.

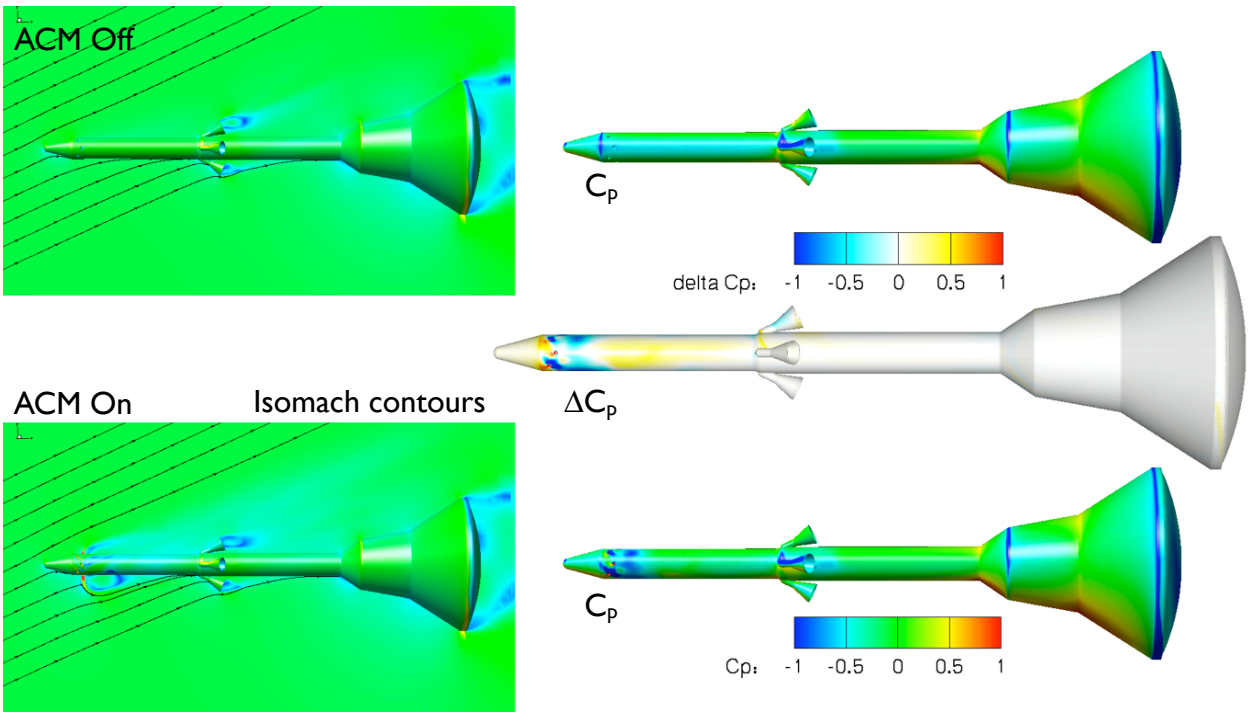

Figure 21: Flow field and load comparison with (lower) and without (upper) ACM jets. Symmetry-plane isomach contours (left), and surface *Cp* contours (right). Delta *Cp* (middle right) is $\Delta Cp = Cp_{ACM\_on} - Cp_{ACM\_off}$. ACM_2.5k, $M_\infty = 0.7$, $\alpha = 25°$.

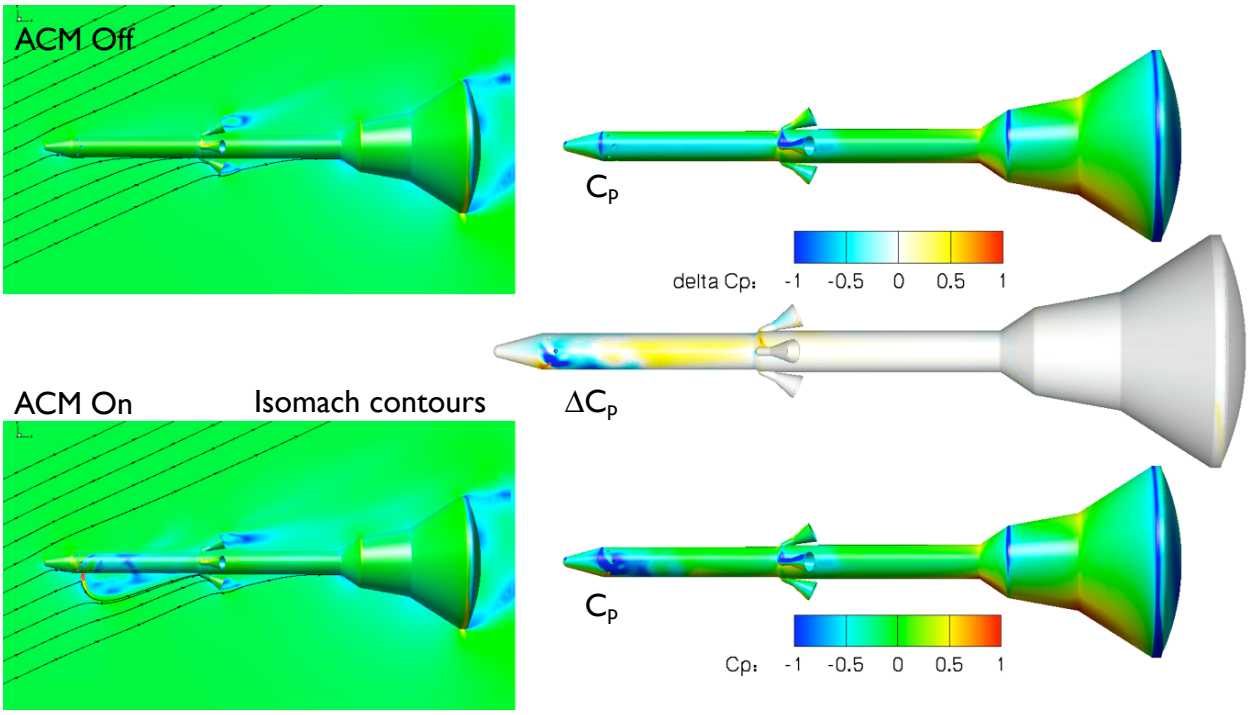

Figure 22: Flow field and load comparison with (lower) and without (upper) ACM jets. Symmetry-plane isomach contours (left), and surface *Cp* contours (right). Delta *Cp* (middle right) is $\Delta Cp = Cp_{ACM\_on} - Cp_{ACM\_off}$. ACM_5k, $M_\infty = 0.7$, $\alpha = 25°$.

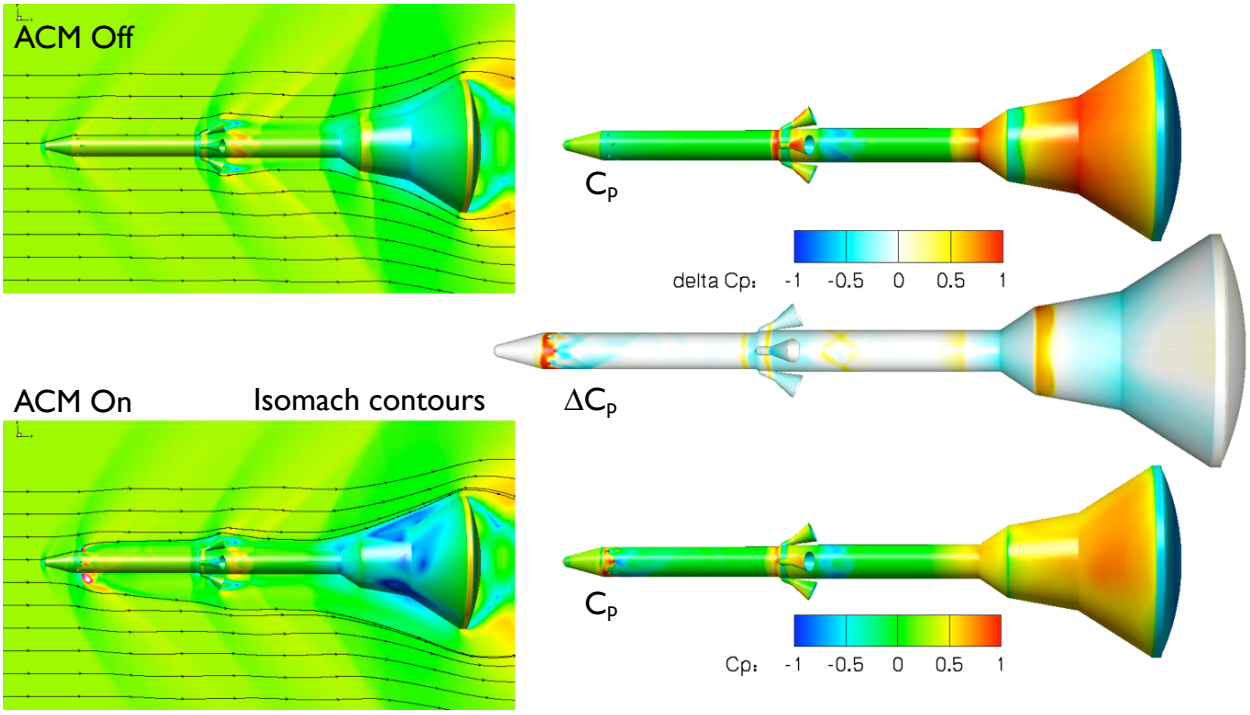

Figure 23: Flow field and load comparison with (lower) and without (upper) ACM jets. Symmetry-plane isomach contours (left), and surface *Cp* contours (right). Delta *Cp* (middle right) is $\Delta Cp = Cp_{ACM\_on} - Cp_{ACM\_off}$. ACM_2.5k, $M_\infty = 1.32$, $\alpha = 0°$.

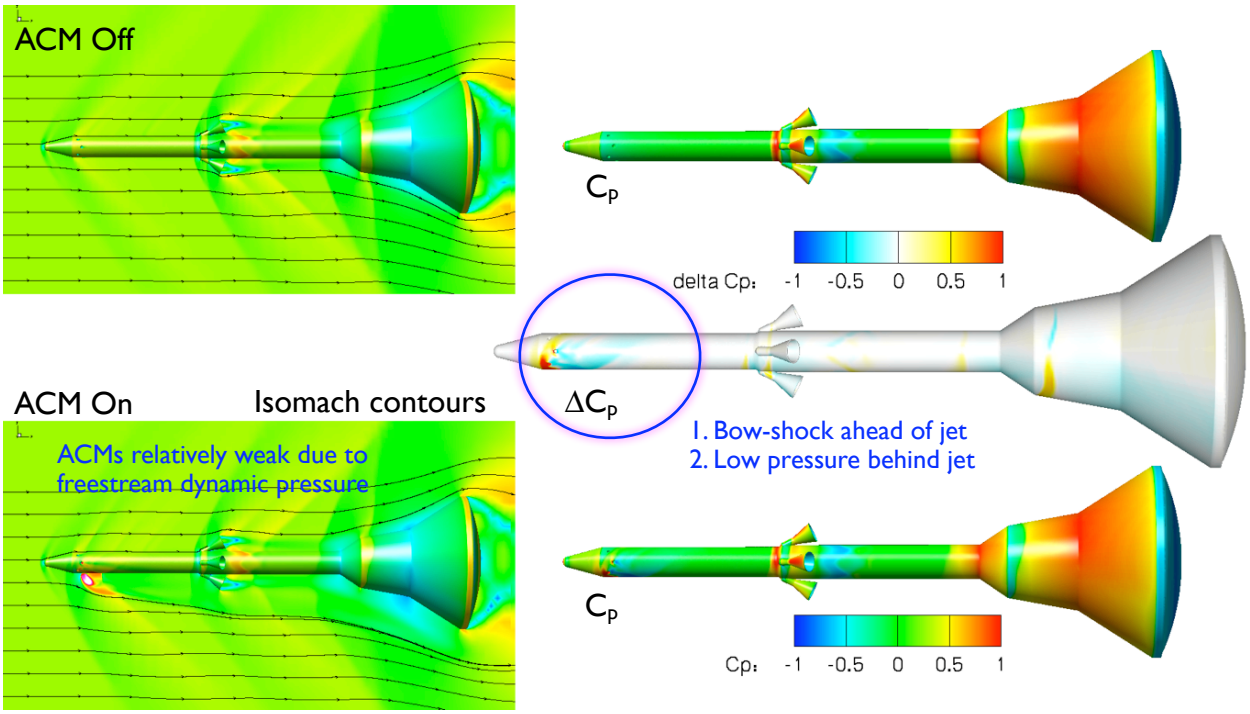

Figure 24: Flow field and load comparison with (lower) and without (upper) ACM jets. Symmetry-plane isomach contours (left), and surface *Cp* contours (right). Delta *Cp* (middle right) is $\Delta Cp = Cp_{ACM\_on} - Cp_{ACM\_off}$. ACM_5k, $M_\infty = 1.32$, $\alpha = 0°$.

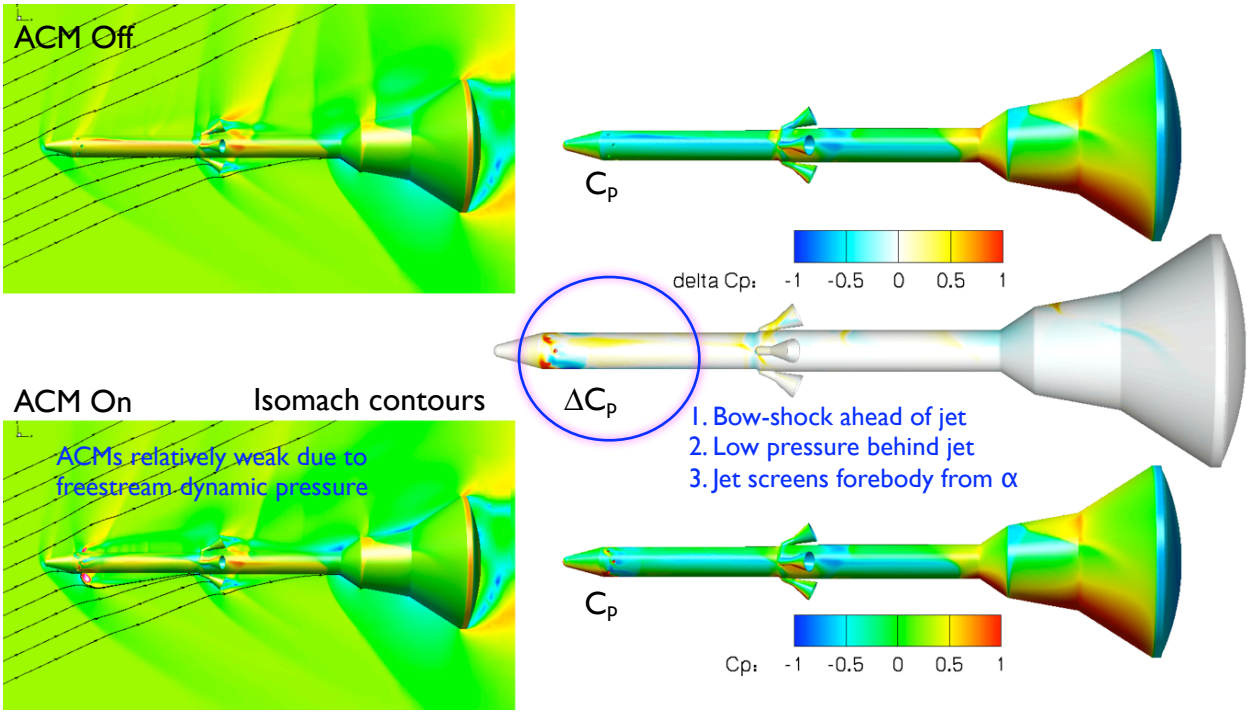

Figure 25: Flow field and load comparison with (lower) and without (upper) ACM jets. Symmetry-plane isomach contours (left), and surface *Cp* contours (right). Delta *Cp* (middle right) is $\Delta Cp = Cp_{ACM\_on} - Cp_{ACM\_off}$. ACM_2.5k, $M_\infty = 1.32$, $\alpha = 25°$.

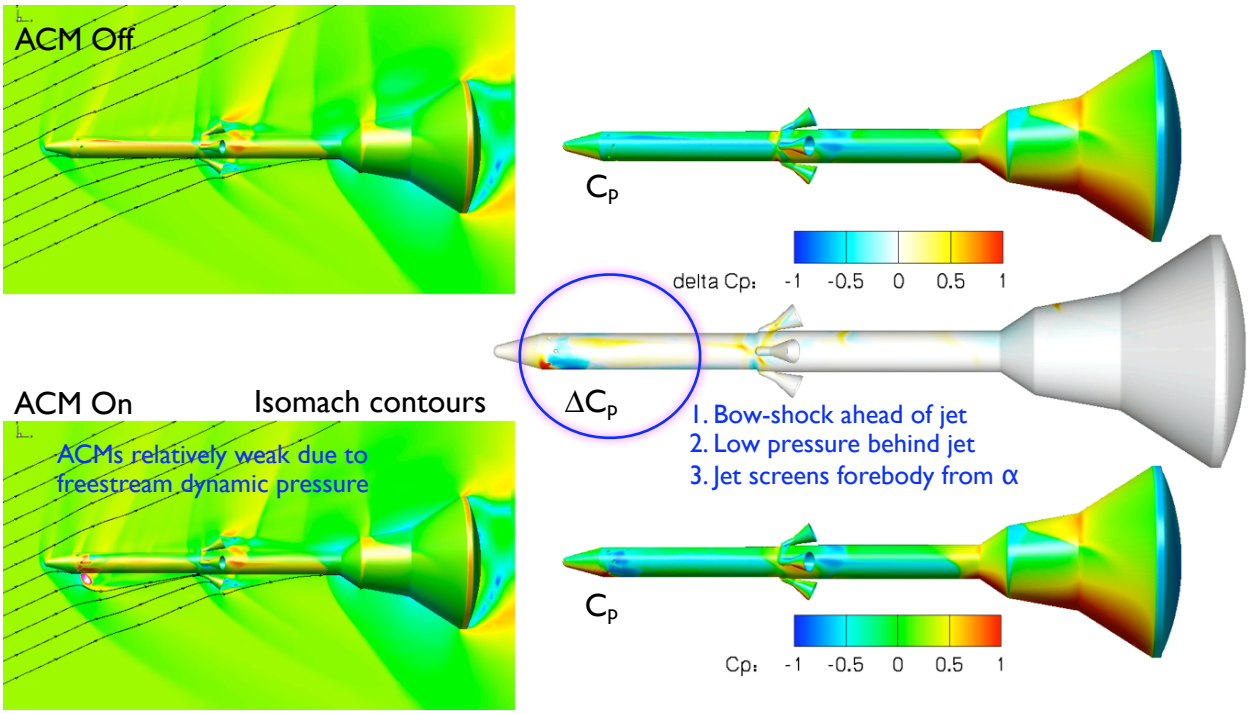

Figure 26: Flow field and load comparison with (lower) and without (upper) ACM jets. Symmetry-plane isomach contours (left), and surface *Cp* contours (right). Delta *Cp* (middle right) is $\Delta Cp = Cp_{ACM\_on} - Cp_{ACM\_off}$. ACM_5k, $M_\infty = 1.32$, $\alpha = 25°$.

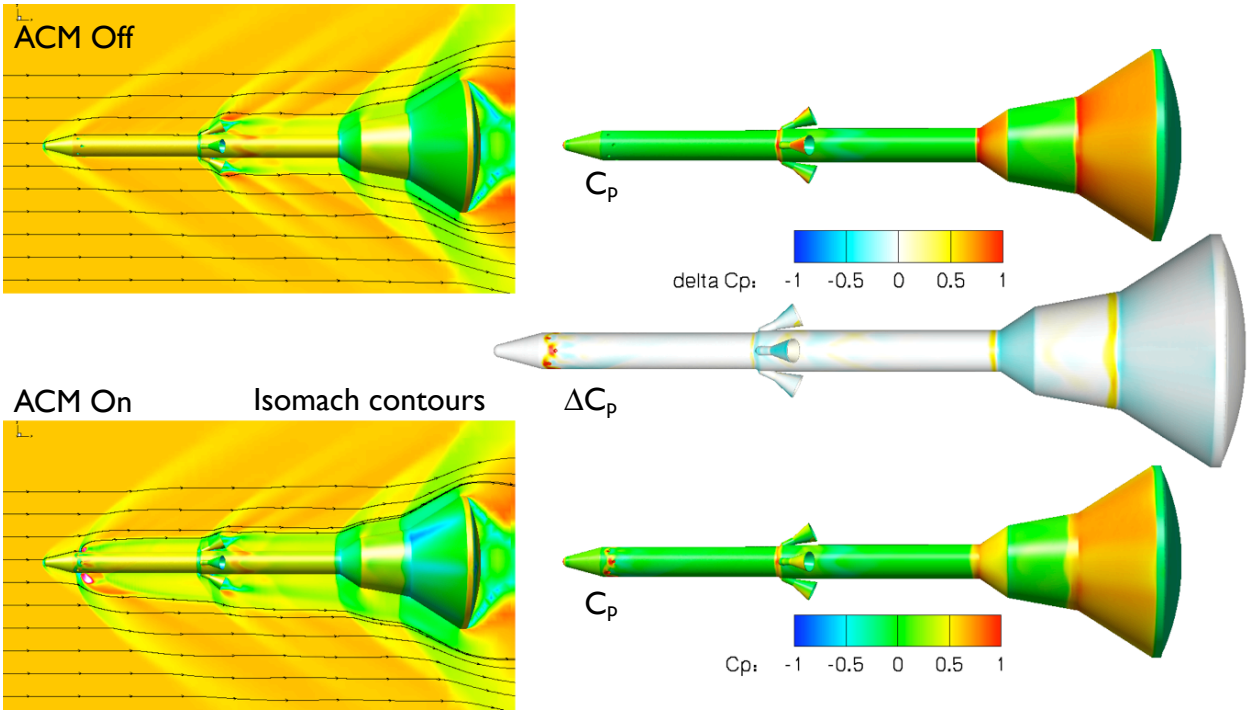

Figure 27: Flow field and load comparison with (lower) and without (upper) ACM jets. Symmetry-plane isomach contours (left), and surface *Cp* contours (right). Delta *Cp* (middle right) is $\Delta Cp = Cp_{ACM\_on} - Cp_{ACM\_off}$. ACM_2.5k, $M_\infty = 2.03$, $\alpha = 0°$.

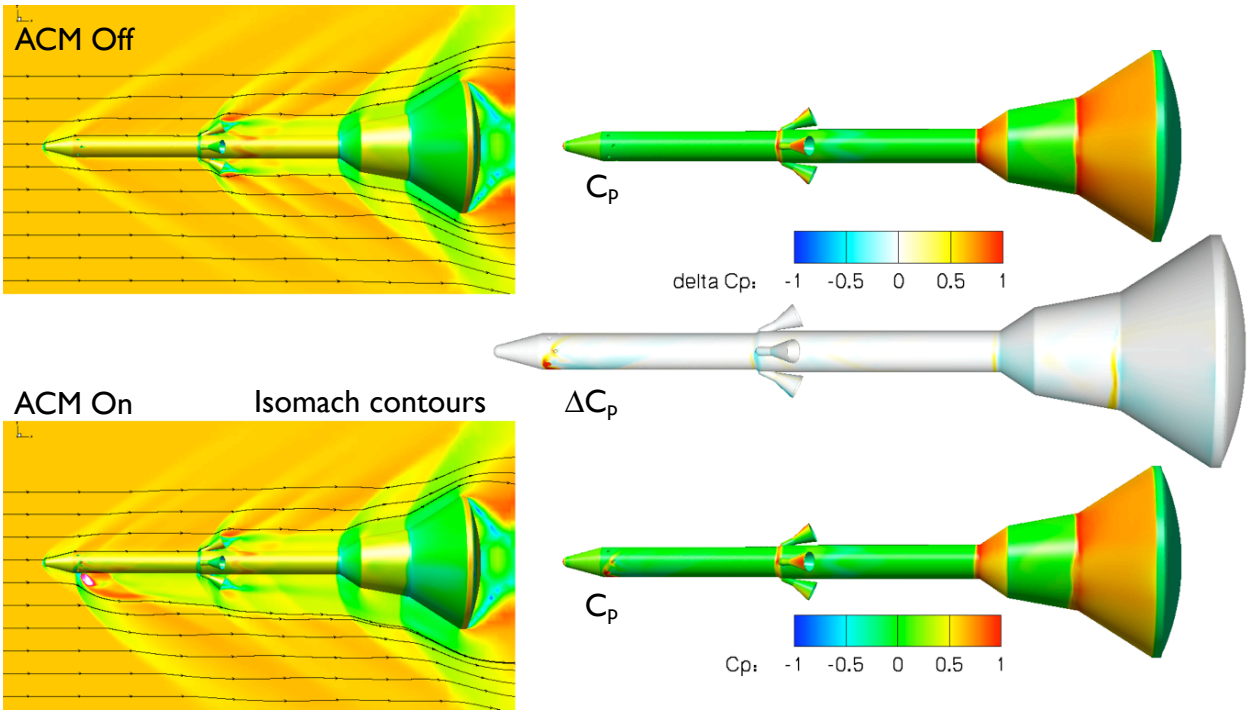

Figure 28: Flow field and load comparison with (lower) and without (upper) ACM jets. Symmetry-plane isomach contours (left), and surface *Cp* contours (right). Delta *Cp* (middle right) is $\Delta Cp = Cp_{ACM\_on} - Cp_{ACM\_off}$. ACM_5k, $M_\infty = 2.03$, $\alpha = 0°$.

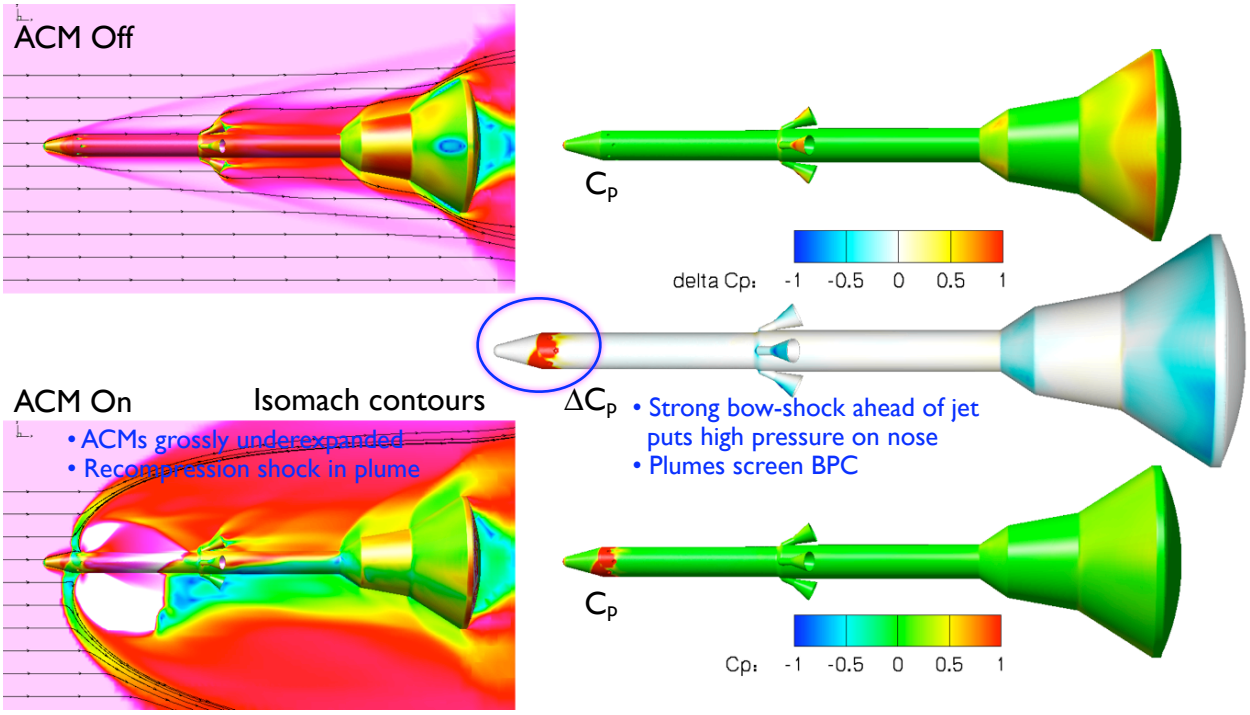

Figure 29: Flow field and load comparison with (lower) and without (upper) ACM jets. Symmetry-plane isomach contours (left), and surface *Cp* contours (right). Delta *Cp* (middle right) is $\Delta Cp = Cp_{ACM\_on} - Cp_{ACM\_off}$. ACM_2.5k, $M_\infty = 6.02$, $\alpha = 0°$.

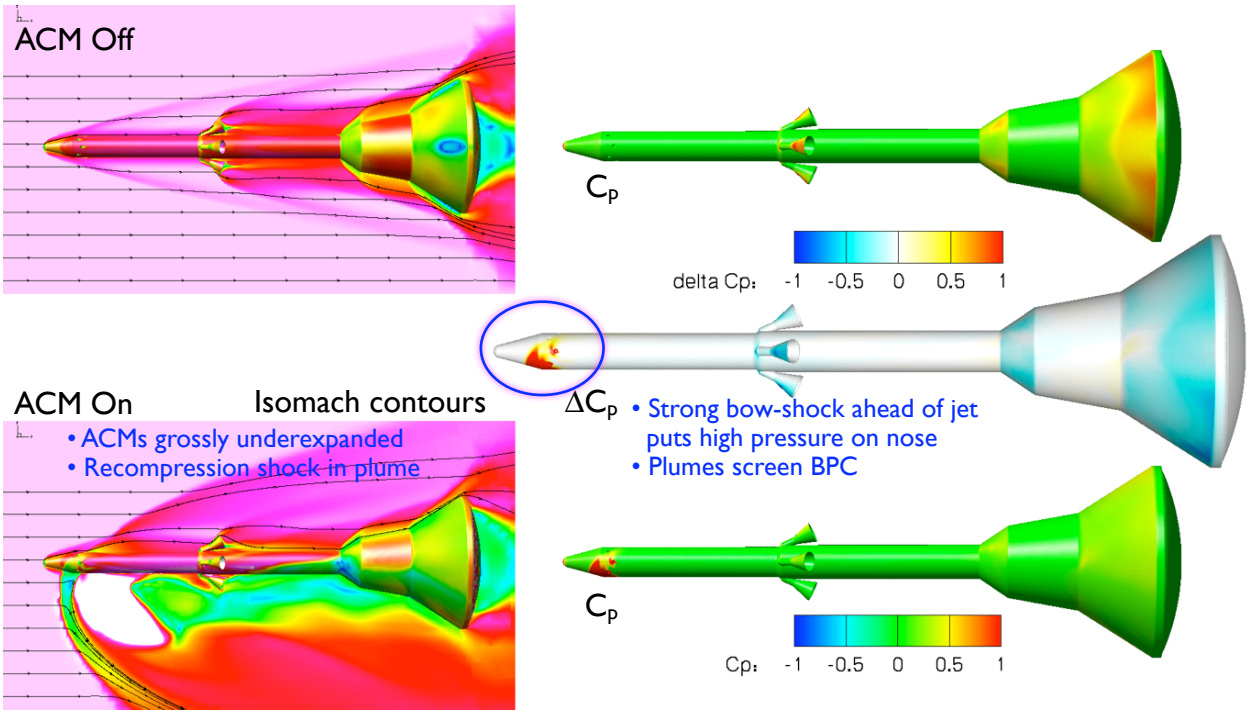

Figure 30: Flow field and load comparison with (lower) and without (upper) ACM jets. Symmetry-plane isomach contours (left), and surface *Cp* contours (right). Delta *Cp* (middle right) is $\Delta Cp = Cp_{ACM\_on} - Cp_{ACM\_off}$. ACM_5k, $M_\infty = 6.02$, $\alpha = 0°$.

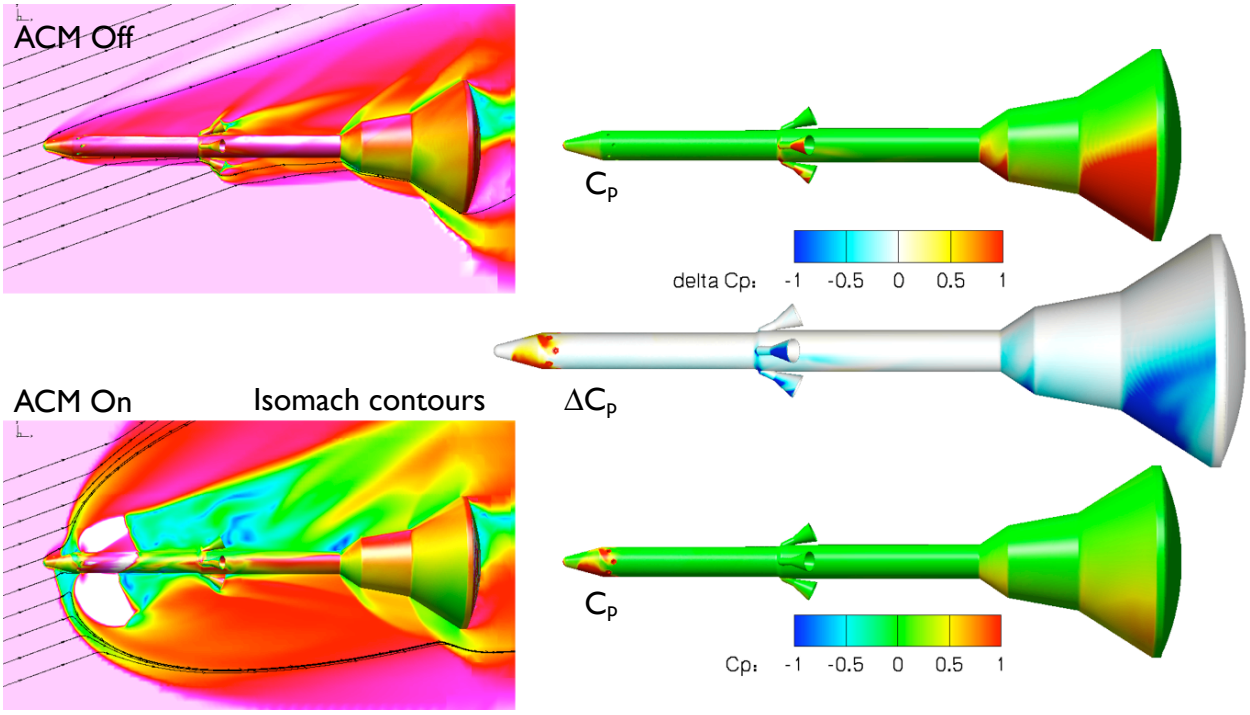

Figure 31: Flow field and load comparison with (lower) and without (upper) ACM jets. Symmetry-plane isomach contours (left), and surface *Cp* contours (right). Delta *Cp* (middle right) is $\Delta Cp = Cp_{ACM\_on} - Cp_{ACM\_off}$. ACM_2.5k, $M_\infty = 6.02$, $\alpha = 20°$.

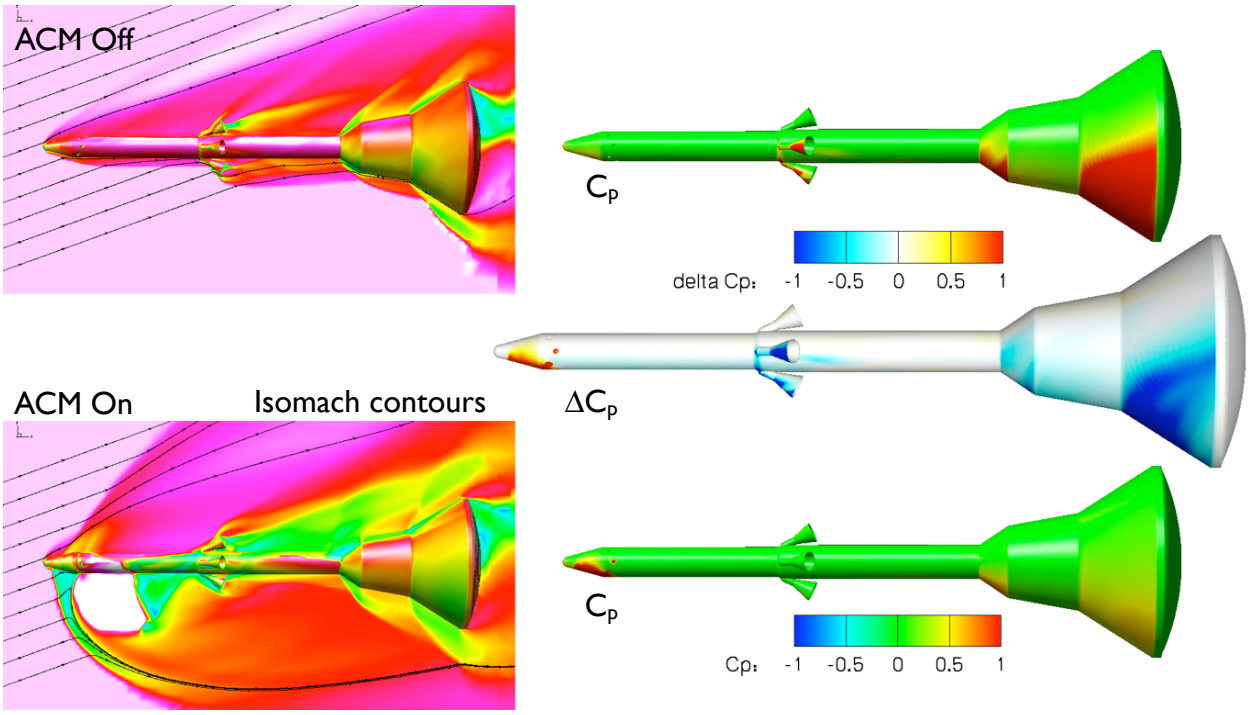

Figure 32: Flow field and load comparison with (lower) and without (upper) ACM jets. Symmetry-plane isomach contours (left), and surface *Cp* contours (right). Delta *Cp* (middle right) is $\Delta Cp = Cp_{ACM\_on} - Cp_{ACM\_off}$. ACM_5k, $M_\infty = 6.02$, $\alpha = 20°$.

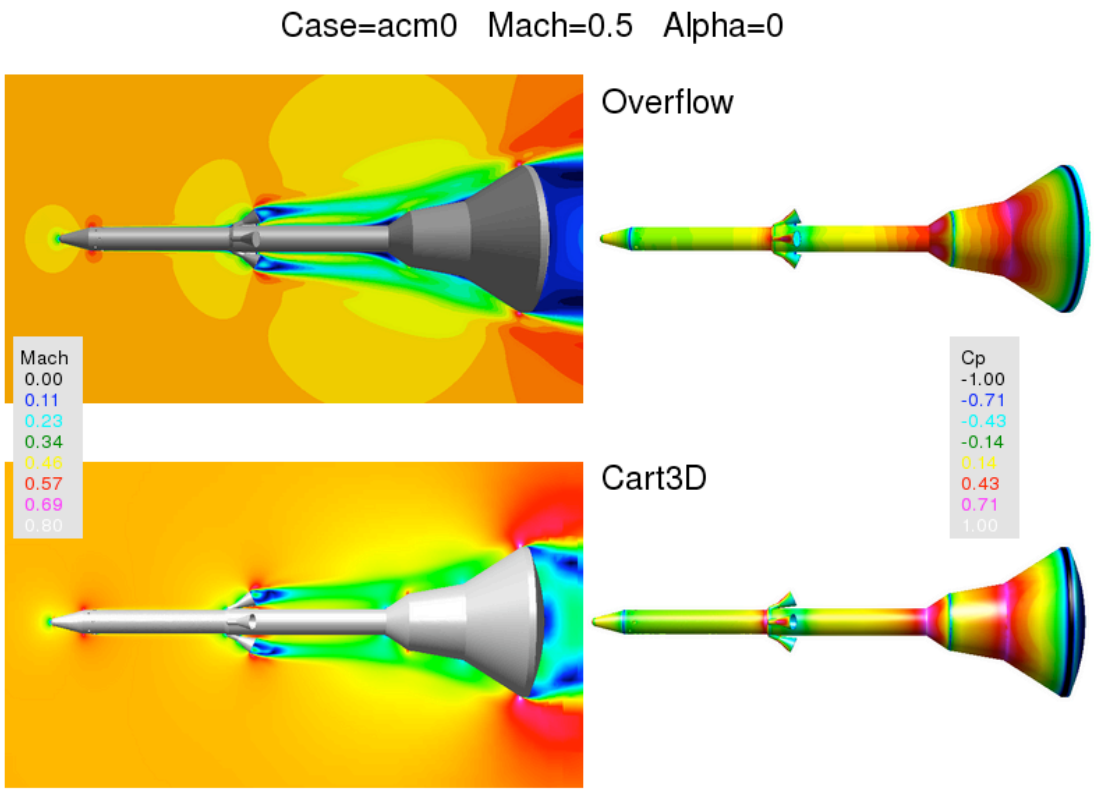

Figure 33: Symmetry plane Mach contours and surface *Cp* distribution comparison of Overflow (top) and Cart3D (bottom) simulations. ACM_off, $M_\infty = 0.5$ $\alpha = 0°$.

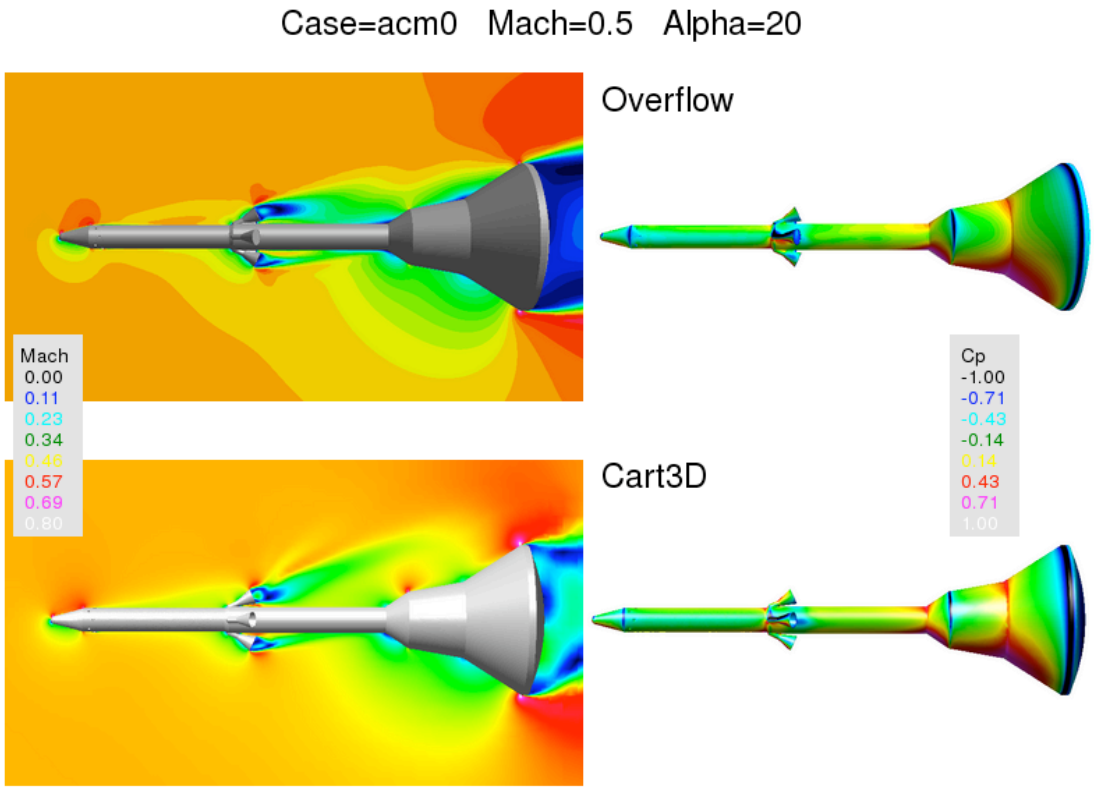

Figure 34: Symmetry plane Mach contours and surface *Cp* distribution comparison of Overflow (top) and Cart3D (bottom) simulations. ACM_off, $M_\infty = 0.5$ $\alpha = 20°$.

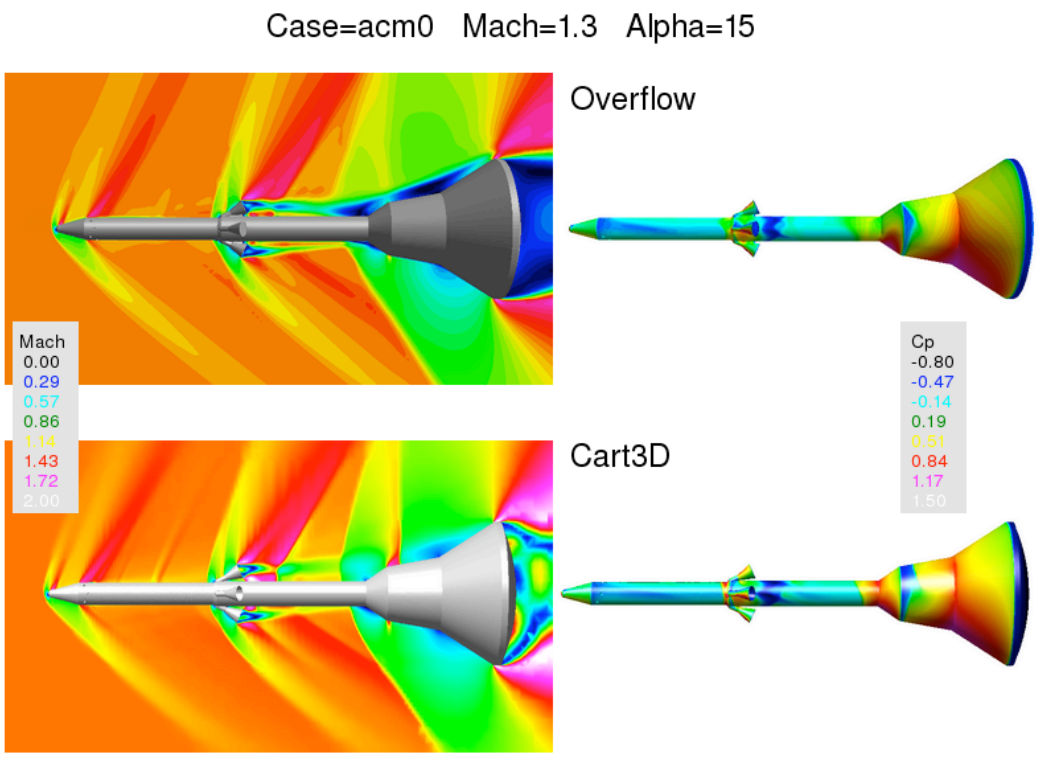

Figure 35: Symmetry plane Mach contours and surface *Cp* distribution comparison of Overflow (top) and Cart3D (bottom) simulations. ACM_off, $M_\infty = 1.3$ $\alpha = 15°$.

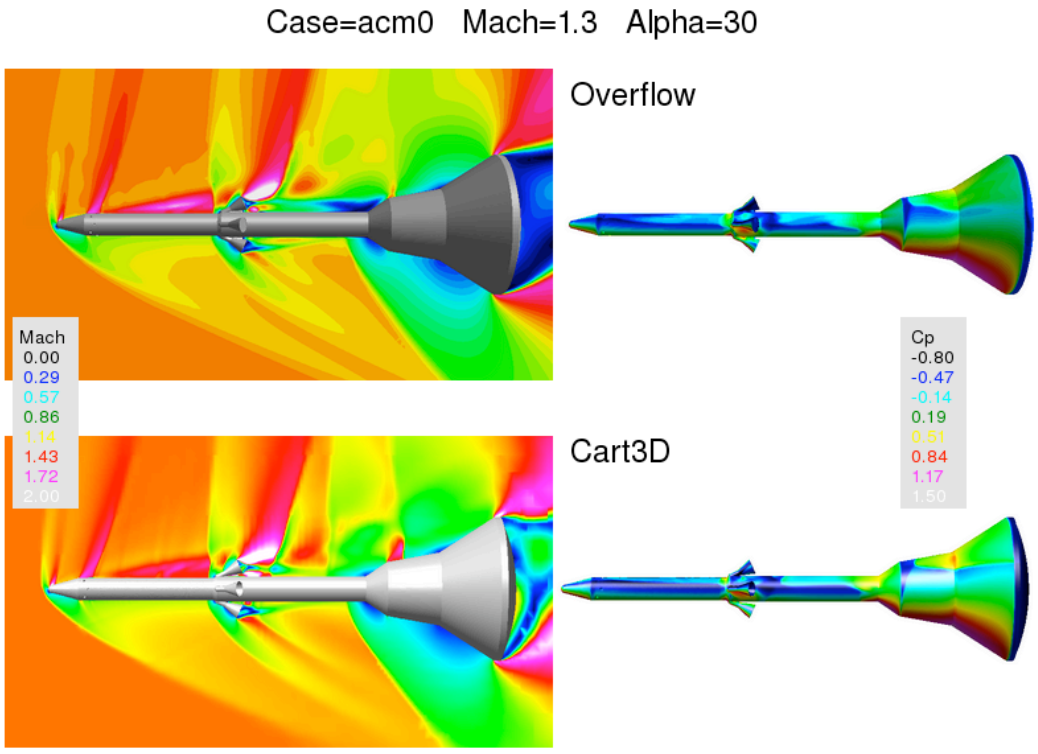

Figure 36: Symmetry plane Mach contours and surface *Cp* distribution comparison of Overflow (top) and Cart3D (bottom) simulations. ACM_off, $M_\infty = 1.3$ $\alpha = 30°$.

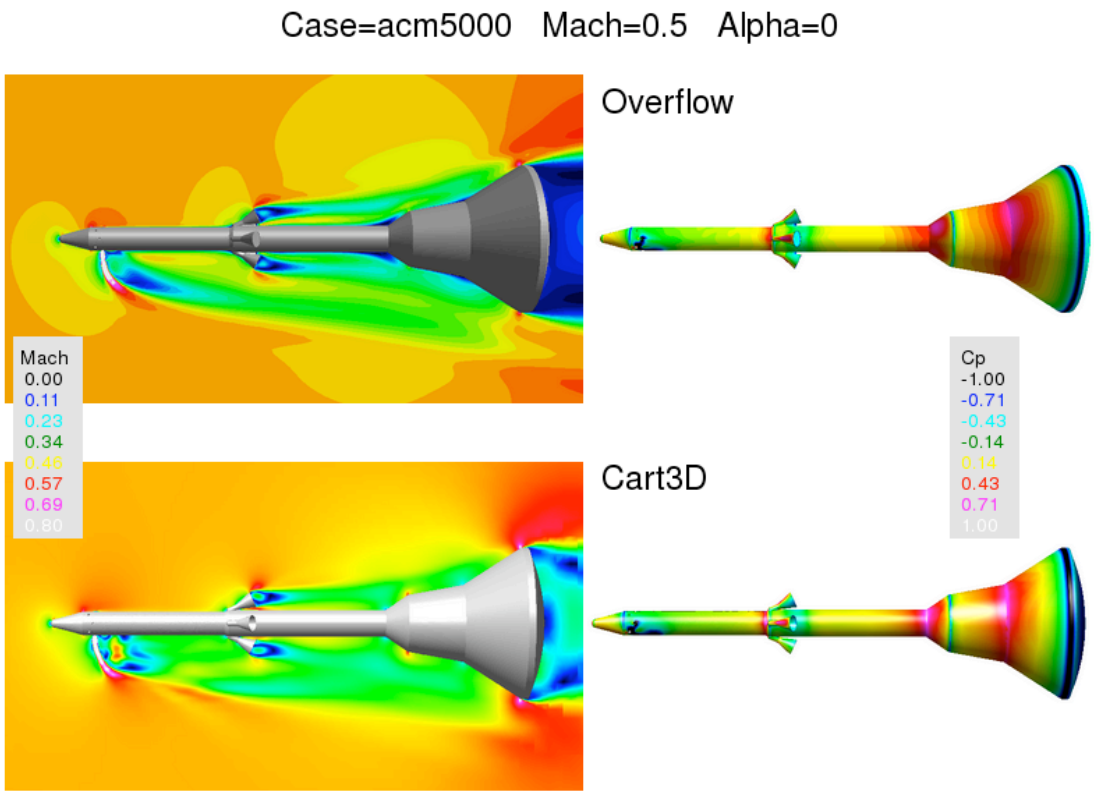

Figure 37: Symmetry plane Mach contours and surface *Cp* distribution comparison of Overflow (top) and Cart3D (bottom) simulations. ACM_5k, $M_\infty = 0.5$ $\alpha = 0°$.

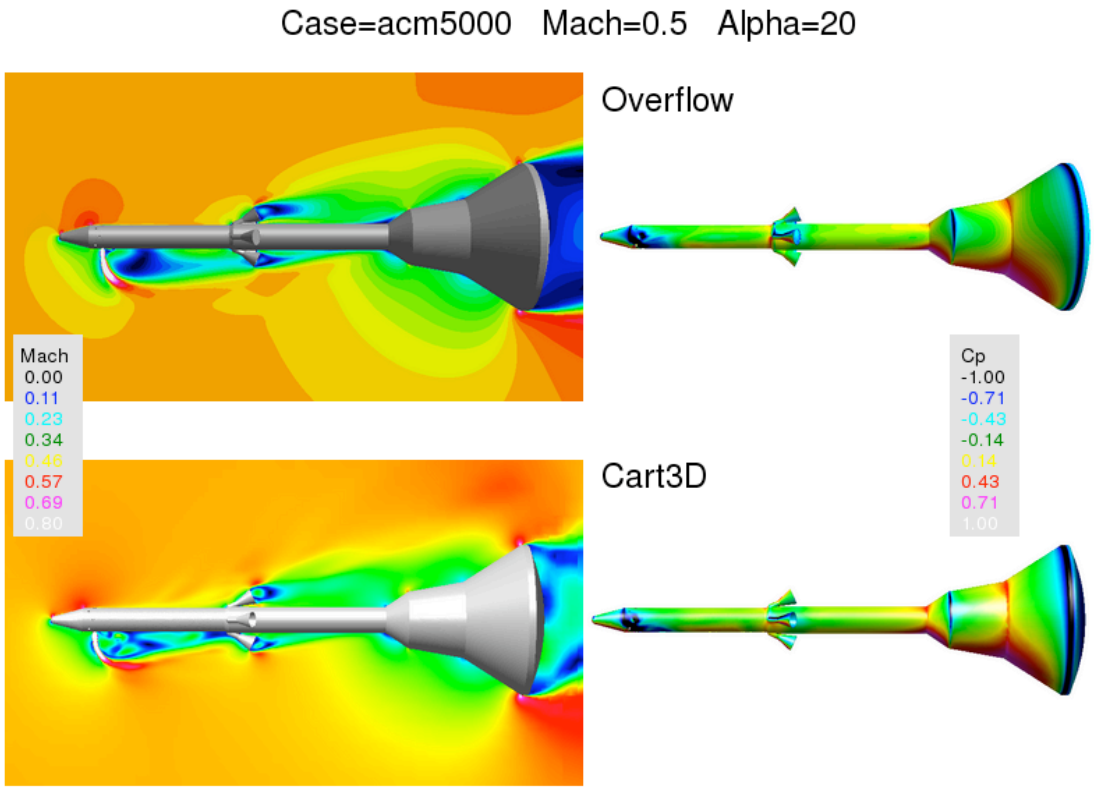

Figure 38: Symmetry plane Mach contours and surface *Cp* distribution comparison of Overflow (top) and Cart3D (bottom) simulations. ACM_5k, $M_\infty = 0.5$ $\alpha = 20°$.

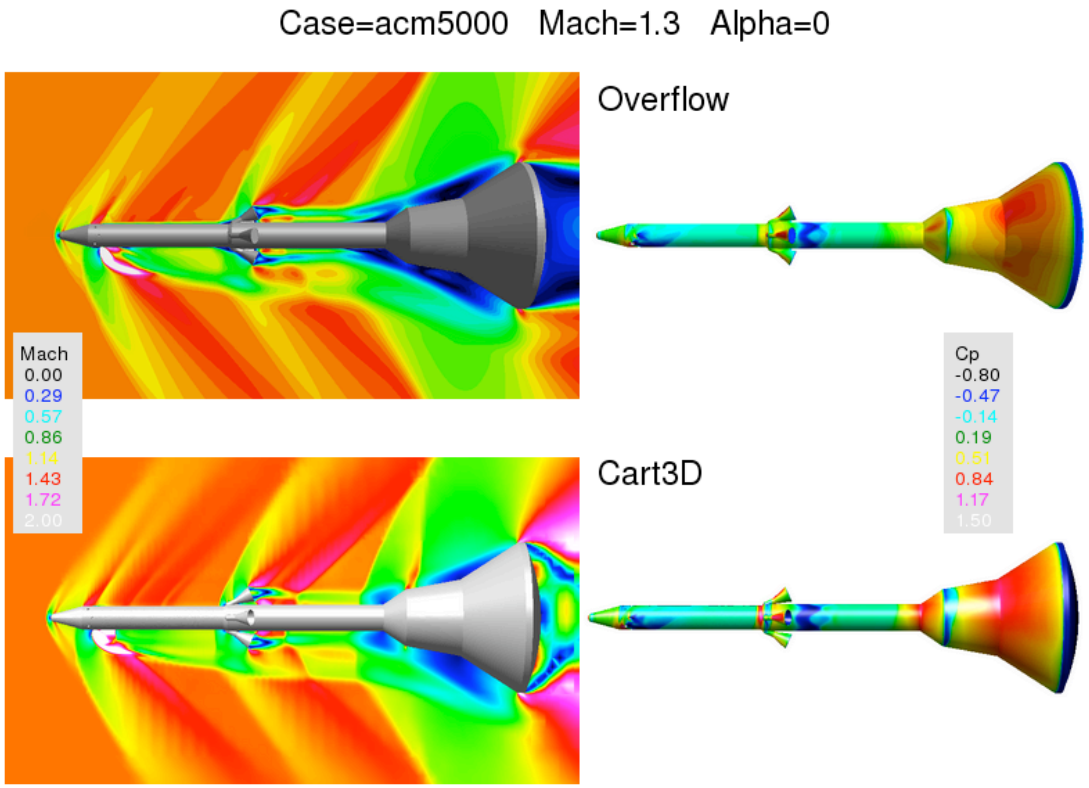

Figure 39: Symmetry plane Mach contours and surface *Cp* distribution comparison of Overflow (top) and Cart3D (bottom) simulations. ACM_5k, $M_\infty = 1.3$ $\alpha = 0°$.

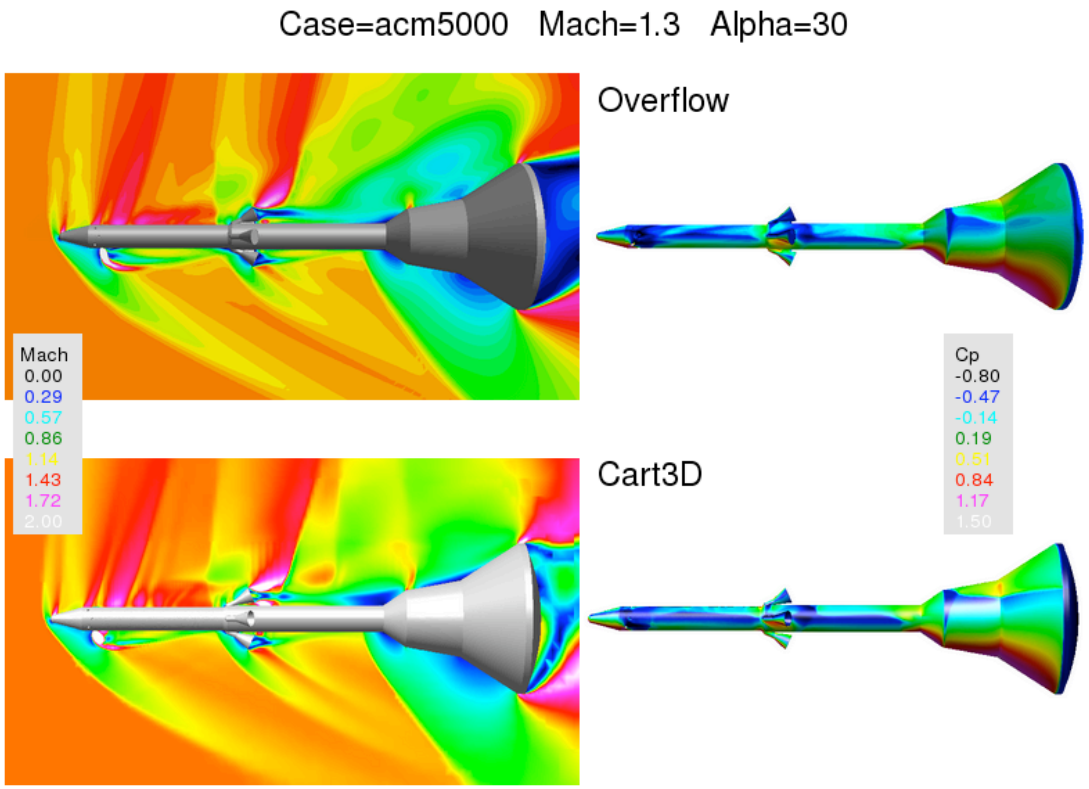

Figure 40: Symmetry plane Mach contours and surface *Cp* distribution comparison of Overflow (top) and Cart3D (bottom) simulations. ACM_5k, $M_\infty = 1.3$ $\alpha = 30°$.

6 Conclusions

Multi-fidelity simulations of a candidate design for the Orion Launch Abort Vehicle were performed in order to study the pitch authority afforded by the Attitude Control Motor system. In total, 653 steady and 16 unsteady inviscid simulations were performed along with 53 full unsteady RANS simulations. These data provide not only a comprehensive vehicle performance database but also give vehicle force and moment deltas for ACM on/off at two levels of ACM thrust. Conditions for the simulations followed the nominal LAV trajectory at 11 Mach numbers in a range from 0.3 to 6.0 with emphasis near Mach 1. Angle-of-attack was varied from -30°to 50° over the entire Mach range, and the simulations considered sideslip angles of 0° and 30°.

As dynamic pressure increases along the trajectory, both simulation codes showed that JI effects become increasingly important relative to fixed levels of ACM thrust. These studies showed that adverse JI occurs at positive angles of attack when the ACM jets screen the LAV tower from the oncoming flow. In particular, adverse JI causes ACM effectiveness to drop rapidly at positive α over Mach numbers from 0.7-1.6, and can result in control reversal for some ACM settings.

Results from the inviscid and viscous simulation codes were compared for a wide variety of flow conditions including sub-, trans-, and supersonic regimes. Both approaches predicted similar losses in ACM effectiveness with the same underlying physical mechanisms. Detailed comparisons of predicted loads were made between the inviscid and RANS simulations. These simulations showed very good agreement for all aerodynamic coefficients with only minor local discrepancies. Design modifications to the Orion LAV enacted since the initial investigations documented in this work have shown that the adverse JI identified herein can be mitigated substantially by relatively minor changes to the arrangement of ACM thrusters.

7 Acknowledgments

The authors gratefully acknowledge direct support from the CEV Aerosciences Project, for their role in this work. We also wish to thank J. Garcia (ARC), J. Olejniczak (ARC) and J. Greathouse (JSC) for providing the LAV geometry and many interesting discussions.

8 References

[1] Aftosmis, M.J., Berger, M.J., and Adomavicius, G. D. “A parallel multilevel method for adaptively refined Cartesian grids with embedded boundaries,” In *Proc. 38th AIAA Aerospace Sciences Meeting & Exhibit, Paper 2000-0808*, Reno, NV, Jan. 2000.

[2] Aftosmis, M.J., Berger, M.J. and Murman, S.M. “Applications of space-filling-curves to Cartesian methods in CFD,” In *Proc. 42nd AIAA Aerospace Sciences Meeting & Exhibit, Paper 2004-1232*, Reno, NV, Jan. 2004.

[3] Berger, M. J., Aftosmis, M.J., Marshall, D. D., and Murman, S. M., "Performance of a new CFD flow solver using a hybrid programming paradigm," *Journal of Parallel and Distributed Computing*, **65**:414–423, 2005.

[4] Aftosmis, M.J., Berger, M.J., and Melton, J.E., "Robust and efficient Cartesian mesh generation for component-based geometry," *AIAA J.* **36**(6):952-960, Jun. 1998.

[5] Mavriplis, D.J., Aftosmis, M.J., and Berger, M.J., "High resolution aerospace applications using the NASA Columbia supercomputer," *International Journal of High Performance Computing Applications*. **21**(1) pp. 106-126. Jan. 2007

[6] Rogers, S.E., "LAV-054 ACM Assessment using OVERFLOW," CEV Aeroscience Project Technical Brief, *EG-CAP-07-45.* Apr. 2007.

[7] Haimes, R., and Aftosmis M.J, "On generating high quality "water-tight" triangulations directly from CAD," *Proc. of the 8th Internat. Grid Conf.*, Honolulu, HI, Jun. 2002.

[8] Melton, J.E., Cliff, S., "CEV CFD simulation guidelines for the CART3D solver," CEV Aeroscience Project Technical Brief, *EG-CAP-06-35 v1.35.* Oct. 2006.

[9] P.G. Buning, R.J. Gomez, and W.I. Scallion, "CFD approaches for simulation of wing-body stage separation," *AIAA Paper 2004-4838*, AIAA 22nd Applied Aerodynamics Conference, Providence, RI, Aug. 2004.

[10] Jespersen, D.C., Pulliam, T.H., and Buning, P.G., "Recent enhancements to OVERFLOW," *AIAA Paper 97-0644,* Jan. 1997.

[11] Rogers, S. E., Roth, K., Nash, S. M., Baker, M. D., Slotnick, J. P., Whitlock, M., and Cao, H. V., "Advances in Overset CFD processes applied to subsonic high-lift aircraft," *AIAA Paper 2000-4216*, Aug. 2000.

[12] Chan, W. M., "The Overgrid interface for computational simulations on overset grids," *AIAA Paper 2002-3188*, June 2002.

[13] Rogers, S. E., Suhs, N. E., and Dietz, W. E. "PEGASUS 5: An automated pre-processor for overset-grid CFD," *AIAA Journal*, **41**(6), June 2003, pp. 1037–1045.

[14] Aftosmis, M.J., "LAV-054 ACM Assessment using Cart3D," CEV Aeroscience Project Technical Brief, *EG-CAP-07-55.* May. 2007.

[15] Aftosmis, M.J., Berger, M.J, Biswas, R., Djomehri, M.J., Hood, R., Jin, H., and Kiris,, "A Detailed Performance Characterization of Columbia using Aeronautics Benchmarks and Applications," *AIAA Paper 2006-0084*, Jan. 2006.